

# Rapid Rotation of *Kepler* field dwarfs and subgiants: Spectroscopic $v \sin i$ from APOGEE

GREGORY V. A. SIMONIAN,<sup>1,2</sup> MARC H. PINSONNEAULT,<sup>2</sup> DONALD M. TERNDRUP,<sup>2</sup> AND  
JENNIFER L. VAN SADERS<sup>3,4,5</sup>

<sup>1</sup>*Department of Physical Science, Concord University, 1000 Vermillion Street, Athens, WV 24712*

<sup>2</sup>*Department of Astronomy, The Ohio State University, 140 West 18th Avenue, Columbus, OH 43210*

<sup>3</sup>*Institute for Astronomy University of Hawai'i Honolulu, HI 96822*

<sup>4</sup>*Observatories of the Carnegie Institution for Science Pasadena, CA 91101*

<sup>5</sup>*Department of Astrophysical Sciences, Princeton University Princeton, NJ 08544*

## ABSTRACT

We use 5,337 spectroscopic  $v \sin i$  measurements of *Kepler* dwarfs and subgiants from the APOGEE survey to study stellar rotation trends. We find a detection threshold of 10 km/s, which allows us to explore the spindown of intermediate-mass stars leaving the main sequence, merger products, young stars, and tidally-synchronized binaries. We see a clear distinction between blue stragglers and the field turnoff in  $\alpha$ -rich stars, with a sharp rapid rotation cutoff for blue stragglers consistent with the Kraft break. We also find rapid rotation and RV variability in a sample of red straggler stars, considerably cooler than the giant branch, lending credence to the hypothesis that these are active, tidally-synchronized binaries. We see clear evidence for a transition between rapid and slow rotation on the subgiant branch in the domain predicted by modern angular momentum evolution models. We find substantial agreement between the spectroscopic and photometric properties of KIC targets added by Huber et al. (2014) based on 2MASS photometry. For the unevolved lower main sequence, we see the same concentration toward rapid rotation in photometric binaries as that observed in rotation period data, but at an enhanced rate. We attribute this difference to unresolved near-equal luminosity spectroscopic binaries with velocity displacements on the order of the APOGEE resolution. Among cool unevolved stars we find an excess rapid rotator fraction of 4% caused by pipeline issues with photometric binaries.

*Keywords:* stars: rotation, stars: late-type

## 1. INTRODUCTION

Rotation is a fundamental property of stars. We observe a wide range of rotation rates in pre-main sequence stars of all masses (Attridge & Herbst 1992; Herbst et al. 2000; Hender-

son & Stassun 2012). Kraft (1967) noticed a dichotomy in rotation rates for stars on the main sequence, with stars more massive than  $1.2M_{\odot}$  maintaining a wide range of rotation rates, while less massive stars rotate substantially slower. The transition between the two is thought to be because of the onset of convective envelopes in lower-mass stars, which lose

angular momentum through magnetized winds (Parker 1958; Weber & Davis 1967; Kawaler 1988). Studying the transition between the two regimes can be a test of wind theory (van Saders & Pinsonneault 2013).

Rotation is valuable for understanding stellar physics not just because it can tell us about stellar dynamos and winds, but also because rotation may yield inferences of stellar ages, a technique known as gyrochronology (Barnes 2007; Mamajek & Hillenbrand 2008). Gyrochronology relations have been calibrated using rotation data from open clusters to infer ages from rotation rates and masses. However, open cluster rotation measurements are primarily in young systems, where amplitudes are high and periods are short, with few old calibrators available. Attempts to calibrate the relations using *Kepler* stars with asteroseismic ages revealed challenges in extending existing gyrochronology relationships. Angus et al. (2015) found that traditional empirical gyrochronology relationships could not be simultaneously fit to young clusters, asteroseismic targets and field stars. A more sophisticated treatment with theoretical models of angular momentum evolution found that *Kepler* asteroseismic stars did not slow down as quickly as predicted by angular momentum models (van Saders et al. 2016). Coincident studies of magnetic activity indicators among *Kepler* asteroseismic stars show that while the rotation of older stars levels off, the magnetic field continues to decrease, suggesting a fundamental change in the magnetic braking mechanism (Metcalfe et al. 2016; van Saders et al. 2016; Metcalfe & van Saders 2017).

Although main-sequence gyrochronology is powerful, there are many other astrophysical problems tied to the study of stellar rotation. Asteroseismology has yielded crucial data on internal stellar rotation in evolved subgiants (e.g. Deheuvels et al. 2014) and red giants (Mosser et al. 2012; Gehan et al. 2018) stars. Measure-

ments of surface rotation rates are important for interpreting the subgiant core rotation data. The advent of *Gaia* parallaxes allows discrimination between dwarfs and subgiants in the *Kepler* field (Berger et al. 2018b).

Close binary stars can be tidally synchronized, and in an earlier paper we found that the short rotation period systems in the *Kepler* lower main sequence are preferentially photometric binaries (Simonian et al. 2019), and are consistent with being a population of tidally-synchronized binaries.

Rotation can be measured in two different ways. One method measures the projected broadening of spectral lines due to rotation (Kaler 1989), which requires spectroscopy. An additional method which has been expanded greatly by the *Kepler* satellite is the measurement of rotation periods through modulations in the light curves due to starspots (see McQuillan et al. 2014; García et al. 2014; Aigrain et al. 2015; Luri et al. 2018, and references therein). These measurements take advantage of long stretches of precise and continuous coverage. Rotational periods are sensitive to much slower rotation rates than  $v \sin i$  because rotational broadening becomes comparable to the few  $\text{km s}^{-1}$  resolution of most high-resolution spectrographs. However, periods can only be measured for cool stars with spots, and detections at low levels become challenging because of systematic uncertainties in the differential photometry (see van Saders et al. 2019 for a discussion)

There is also little known about how the behavior of stellar rotation changes with metallicity. Angular momentum evolution models are largely based on open clusters with metallicities in the range of  $-0.01 \leq [\text{Fe}/\text{H}] \leq 0.16$  (Netopil et al. 2016). Multiplexed high-resolution spectroscopy, such as that done by the Apache Point Galactic Evolution Experiment (APOGEE) will

be useful for measuring metallicity and  $v \sin i$  simultaneously for large samples.

While there have been several attempts to validate the rotation periods of *Kepler* stars by cross-comparisons of different periodogram analyses (see Aigrain et al. 2015), there have been few efforts to do so with independent measures such as  $v \sin i$  (see Gilhool et al. 2018, for a comparison in M dwarfs). The advent of large spectroscopic surveys, such as the APOGEE, has enabled the measurement of  $v \sin i$  for hundreds of thousands of stars.

In this paper, we compare the rotation distribution of *Kepler* targets to that seen from APOGEE  $v \sin i$ . Section 2 describes the sample selection as well as the methodology used in this analysis. Section 3 describes the validation done for the APOGEE  $v \sin i$ . Section 4 presents the main science results for the *Kepler* subgiants. We then discuss the implications of the study and conclude in Section 5.

## 2. METHODS

In this work, we compare APOGEE  $v \sin i$  to *Kepler* rotation periods and to models of stellar rotation. In order to perform these comparisons, we supplement rotation data with stellar properties, such as temperature, stellar radius, metallicity, and luminosity. We begin by describing the sources of data for our primary analysis, the sample selection for our main science sample, and finally describing methods and additional datasets for data validation.

### 2.1. Fundamental Stellar Properties

The stellar parameters we are interested in are temperature, chemical abundance, luminosity, and radius. While some are measured directly from the spectra, others need to be inferred indirectly. We describe how these parameters are derived in detail below.

#### 2.1.1. Effective Temperature, Metallicity, and Alpha Enhancement

The underlying sample is drawn from Data Release 14 (Abolfathi et al. 2018) of the Sloan Digital Sky Survey (SDSS) (Majewski et al. 2017), hereafter DR14. Our data is obtained with the APOGEE spectrograph, a critically-sampled high-resolution ( $R \sim 22,000$ ) multi-fiber near-infrared ( $1.51\text{--}1.70\mu\text{m}$ ) spectrograph (Wilson et al. 2010) mounted on the SDSS 2.5-meter telescope at Apache Point Observatory (Gunn et al. 2006). The APOGEE Stellar Parameters and Chemical Abundances Pipeline (ASPCAP) measures stellar parameters, such as  $T_{\text{eff}}$ ,  $[\text{Fe}/\text{H}]$ , and  $[\alpha/\text{Fe}]$ , as well as rotational broadenings by fitting the APOGEE spectra to a grid of stellar atmosphere models.

Serenelli et al. (2017) compared APOGEE DR13  $T_{\text{eff}}$  and  $[\text{Fe}/\text{H}]$  values for the APOGEE-*Kepler* Asteroseismic Science Consortium (APOKASC) dwarfs and subgiants to those measured from high-resolution optical spectroscopy and found that the temperatures were consistent within the uncertainties of around 80 K, with a possible 20 K zero-point shift, which is very small for our purposes. However, they claimed that the reported uncertainty in  $[\text{Fe}/\text{H}]$  was underestimated, and the true random error was closer to 0.1 dex. No analogous analysis was performed in DR14, and we therefore adopt the Serenelli et al. (2017) errors.

#### 2.1.2. Binarity

Most stars are found in binary systems (Moe & Di Stefano 2017), and main sequence binaries have been shown under some circumstances to yield biased stellar parameters when analyzed as single stars (El-Badry et al. 2018a; Simonian et al. 2019). By contrast, the steeply mass-dependent main-sequence lifetime means that evolved primaries in binaries are more luminous than their companions, so the impact of binarity is reduced. In our sample, we can compare the impact of binarity on stellar parameters of evolved stars compared to those near the main sequence. We use two main methods to flag bi-

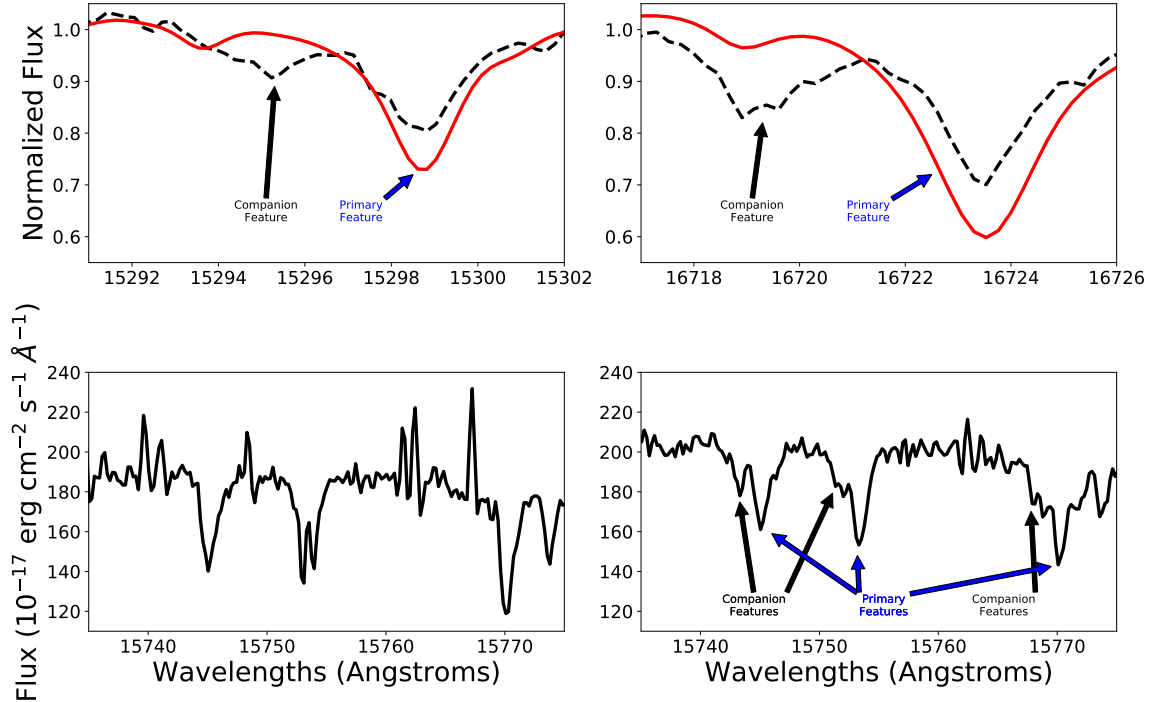


**Figure 1.** Illustrative examples of visual SB2s. *Top Left:* Combined spectrum for KIC 11856076 centered on 15296.5 Å. Two features are separated by 3.5 Å. The combined APOGEE spectrum is shown as a dashed black line, while the best-fit ASPCAP spectrum is shown as a solid red line. *Top Right:* Same spectrum as top left except centered on 16721.5 Å. There are also two features which are separated by approximately 4 Å. *Bottom Left:* Visit spectrum for KIC 7663322 in region centered on 15755 Å containing many features. *Bottom Right:* Visit spectrum taken 538 days later with second component visible.

naries in our sample: visual inspection of the spectra for SB2s, and inference of photometric binaries from excess luminosity above the lower main sequence.

**Double-Lined Spectroscopic Binaries (SB2):** One potentially significant class of contaminants are SB2s. The ASPCAP pipeline assumes a single-star stellar atmosphere to derive stellar parameters. If a spectrum has two sets of lines, ASPCAP will attempt to fit an extremely broad single line profile on top of both sets of lines, resulting in a spurious rapid rotation measurement. We visually inspected the spectra of all targets in our sample with  $v \sin i$  greater than  $10 \text{ km s}^{-1}$  (the detection threshold determined in Section 3.1.2), and flagged them if the star showed signatures of double-lined spectra either in the combined spectrum, or in any of the individual visit spectra. An illustra-

tive example of each case is shown in Fig. 1. As expected, we find evidence that the SB2s have overestimated  $v \sin i$  compared to rotation periods in Section 3.1.3.

**Photometric Binaries:** We separate photometric binaries from single stars on the lower main sequence following the methodology described in Simonian et al. (2019), using the conservative threshold of 0.3 mag above the main sequence. One difference in methodology is that we adopt version 1.2 of the MIST isochrones (described in Section 2.1.4) instead of version 1.1.

We impose an upper limit of luminosity at  $-1.3 \text{ mag}$  above the main sequence, which corresponds to three times the main-sequence luminosity. This ceiling leaves ample room for excess luminosity in potential triple systems (Simonian et al. 2019). Targets more luminous than

this ceiling are labeled as “sub-subgiants” (see Fig. 4), and they are discussed in Section 4.3.

### 2.1.3. Luminosity

We calculate bolometric luminosity by combining *Gaia* parallaxes with 2MASS *Ks* photometry (Skrutskie et al. 2006) and extinction estimates from Berger et al. (2018b), and then adding in a *Ks*-band bolometric correction. Anytime we illustrate the sample in an HR diagram, we use the de-reddened *Ks*-band luminosity as a precise marker of evolutionary state, minimizing the impact of extinction.

We also use high-quality parallaxes from the *Gaia* mission’s Data Release 2 (Gaia Collaboration et al. 2018). We match *Kepler* targets against *Gaia* DR2 using the cross-matched database of Berger et al. (2018b), which contains all but 778 out of the 16,915 *Kepler* targets in DR14. The missing targets can be attributed to the quality cuts in Berger et al. (2018b)<sup>1</sup>. Because Berger et al. (2018b) only included targets with low parallax uncertainties, we use the traditional formula for deriving distance modulus from parallax instead of the Bayesian method advocated by Luri et al. (2018) to reduce computational complexity. We include a zero-point offset of 50.2  $\mu$ as determined from comparisons to asteroseismic radii (Zinn et al. 2019).

We use estimates of extinction from the Berger et al. (2018b) catalog, which are based on the 3-D reddening map of Green et al. (2018). We convert the extinction to  $A_K$  using the Cardelli et al. (1989) relation that  $A_K/A_V = 0.114$ .

To get the bolometric absolute magnitude, we add  $M_{K_s}$  to the bolometric correction calculated by interpolating the ATLAS12/SYNTHETIC Kurucz (1970, 1993) stellar atmosphere models in-

<sup>1</sup> Berger et al. (2018b) excluded targets with parallax errors greater than 20%,  $T_{\text{eff}} < 3000$  K,  $\log(g) > 0.1$  dex, and targets with less than “AAA”-quality 2MASS photometry

cluded with the MIST isochrones over  $T_{\text{eff}}$  and  $[\text{Fe}/\text{H}]$ .

A very small fraction of targets (0.3%) of the APOGEE sample have 2MASS photometry flagged due to blending. We exclude these stars.

### 2.1.4. Radius

**Single Stars:** We first calculate isochrone-independent radii by making use of the bolometric luminosity and temperature through the Stefan-Boltzmann law. Calculating radii makes use of the bolometric absolute magnitude from Section 2.1.3, and the effective temperature, which are available in the combined APOGEE/*Gaia*/2MASS catalogs.

**Photometric Binaries:** The above method will yield incorrect radii for unresolved photometric binaries because the Stefan-Boltzmann law assumes all of the flux comes from a single star. Excess luminosity from a binary companion will result in the radius of the primary star being overestimated. In general, radii depend on both effective temperature and age, so we cannot easily disentangle evolved subgiants from photometric binaries. However, on the unevolved lower main sequence ( $T_{\text{eff}} < 5250$  K; see Simonian et al. 2019), age effects are small and we can use the main-sequence radius-effective temperature relationship to estimate the true radii. We perform this correction by projecting the observed *Ks*-band absolute magnitude onto a 1 Gyr,  $[\text{Fe}/\text{H}] = 0.08$  MIST isochrone at fixed  $T_{\text{eff}}$ , as done in Simonian et al. (2019).

## 2.2. The APOGEE-Kepler Dwarf and Subgiant Sample

We focus on the sample of *Kepler* stars observed by APOGEE as of DR14 (Zasowski et al. 2017). The majority of the *Kepler*-APOGEE targets were chosen for asteroseismic studies of evolved red giants, but 7,918 unevolved stars were targeted by the survey, and 5,337 were observed as of DR14.

**Table 1.** APOGEE Targeting Flags

Targeting Flag	Total	Dwarfs/Subgiants
APOGEE_KEPLER_COOLDWARF	702	598
APOGEE2_APOKASC_DWARF	2303	2265
APOGEE2_APOKASC_GIANT	4114	388
APOGEE2_KOI	340	329
APOGEE2_KOI_CONTROL	38	36
APOGEE_KEPLER_SEISMO	7509	1486
APOGEE_RV_MONITOR_KEPLER	163	162
APOGEE_KEPLER_HOST	111	108
Total	15242	5337

NOTE— Number of stars in each APOGEE targeting program as of DR14, and those that pass the Dwarf/subgiant cut. Some stars were targeted in multiple programs, so the total sample will be less than the sum of all targeting flags.

The majority of our targets were taken from magnitude and color selected samples of dwarfs and subgiants, supplemented by a smaller asteroseismic data set. We also included several smaller surveys which targeted dwarfs. For full details about the targeting in APOGEE, we refer the reader to the APOGEE targeting page<sup>2</sup>, as well as [Zasowski et al. \(2017\)](#). We provide a brief overview of the selection functions here.

Stars targeted for specific science programs in APOGEE are flagged as such. The programs we draw from are briefly described here, and listed in Table 1. The APOGEE\_KEPLER\_COOLDWARF targets are bright ( $H \leq 11$  mag), with [Pinsonneault et al. \(2012\)](#)  $T_{\text{eff}} < 5250$  K and [Brown et al. \(2011\)](#)  $\log(g) > 4.0$ . APOGEE2\_APOKASC targets extended this sample to hotter temperatures and lower surface gravities based on [Pinsonneault et al. \(2012\)](#)  $T_{\text{eff}}$  and [Huber et al. \(2014\)](#)  $\log(g)$ . APOGEE2\_APOKASC is made up of APOGEE2\_APOKASC\_GIANT, which selects stars with  $T_{\text{eff}} < 5500$  K and  $\log(g) <$

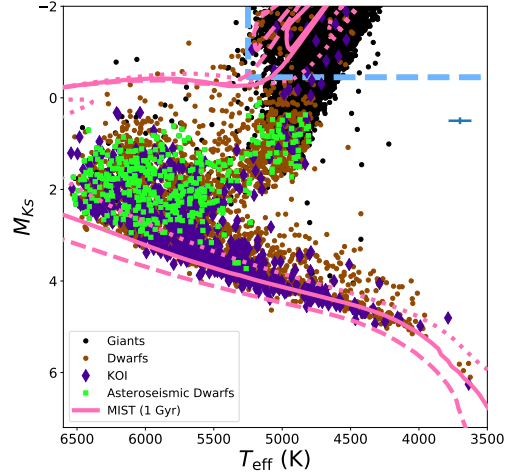


**Figure 2.** The APOGEE sample based on targeting flags. Stars flagged as part of the giant sample as black dots, dwarf sample as red dots, and *Kepler* Objects of Interest as purple diamonds (see text for details). Targets with asteroseismic radii analyzed in [Serenelli et al. \(2017\)](#) are marked as green triangles. Our selection cut for giants is shown as the blue dashed line. A representative error bar is shown in the top right. 1 Gyr MIST isochrones for metallicities  $[\text{Fe}/\text{H}] = -0.5, 0.0,$  and  $0.5$  are shown in pink dashed, solid, and dotted lines, respectively.

3.5, and APOGEE2\_APOKASC\_DWARF, which selects stars with  $6000 \text{ K} > T_{\text{eff}} > 4500 \text{ K}$ . APOGEE\_KEPLER\_SEISMO targets were selected to follow-up stars showing asteroseismic oscillations in *Kepler*. Most of this sample is giants, but 426 stars were dwarfs targeted for asteroseismic studies ([Chaplin et al. 2011](#)). APOGEE2\_KOI and APOGEE2\_KOI\_CONTROL were selected to follow-up *Kepler* planet host stars. The number of stars in our sample from each of the targeting programs is shown in Fig. 2.

After gathering all targets from Table 1, we remove giants by imposing a cut on targets with  $T_{\text{eff}} < 5250$  K and  $M_{Ks} < -0.45$ , shown in Fig. 2. This cut is more inclusive of the base of the RGB than a traditional spectroscopic  $\log(g) > 3.5$  cut. However, we choose to be more inclusive because of the discovery of a

<sup>2</sup> <https://www.sdss.org/dr14/irspec/targets/>

population of potential red stragglers (see Section 4.3). While [Tayar et al. \(2015\)](#) has done a more thorough investigation of the giants which is not our focus, the APOGEE sample at the time of that study was not large enough to reveal this red straggler population. The number of dwarfs and subgiants passing this cut are we also listed in Table 1.

Our final dwarf/subgiant sample has the following properties:  $7 \leq H \leq 14$ . The typical range of parallaxes (with  $1\sigma$  quartile ranges) is  $1.86_{-1.02}^{+2.55}$  mas. The median extinction for our sample of dwarfs and subgiants is  $0.013_{-0.006}^{+0.014}$  mag.

[Huber et al. \(2014\)](#) added stars to the KIC with saturated KIC photometry by leveraging 2MASS colors. Because APOGEE used the [Huber et al. \(2014\)](#) catalog for selection, it targeted a substantial fraction of these stars—34%—which did not previously have stellar parameter estimates. We evaluate the reliability of the [Huber et al. \(2014\)](#) methodology in Appendix A.

### 2.2.1. Spectroscopic Flags and Quality Cuts

The ASPCAP pipeline infers stellar parameters ([García Pérez et al. 2016](#)) by fitting a 6-dimensional grid of stellar atmospheres to the APOGEE spectra ([Allende Prieto et al. 2006](#)). This fit failed significantly for 2.6% of our sample and triggered the STAR\_BAD quality flag<sup>3</sup>. Less extreme discrepancies can trigger the STAR\_WARN flag. Visual inspection of a representative sample of targets with STAR\_WARN indicated reasonable fits, so we included these

<sup>3</sup> The STAR\_BAD flag is triggered if any of the stellar parameters are near the grid edge, the combined S/N of the spectrum is less than 50, the chi-square of the fit is greater than 50, or the derived spectroscopic temperature is discrepant from the [González Hernández & Bonifacio \(2009\)](#)  $J - K$  color temperature by more than 500 K. For more information see the APOGEE documentation at <https://www.sdss.org/dr14/irspec/parameters/>.

targets and excluded almost all objects with the STAR\_BAD flag.

However, there are 13 objects in our sample where the STAR\_BAD flag was only triggered because the  $v \sin i$  hit an upper grid edge in the fit. To avoid preferentially excluding rapid rotators, we manually calibrate stellar parameters for these stars ([Holtzman et al. 2018](#)), and treat those few targets as  $v \sin i$  lower limits. This sample is so small that inclusion of these stars do not substantially affect our conclusions.

## 2.3. Validation Datasets

Some of the data used in Section 2.1 is relatively new and has not been extensively validated, we perform additional validation by supplementing these data with that from other studies. Comparison to rotation periods is a major part of our validation, but we also supplement with other datasets of radius, binarity and temperature. For a summary of the validation tables, and the size of their overlap with the APOGEE rotation sample, see Table 2.

### 2.3.1. Rotation

The APOGEE  $v \sin i$  measurements were only included as catalog values as of DR14. As a result, they have not been thoroughly validated. [Tayar et al. \(2015\)](#) measured  $v \sin i$  directly from the APOGEE spectra and showed that rapid rotation could be successfully measured in giants. We extend this validation into the dwarf and subgiant regime by comparing to rotation periods, as well as to literature  $v \sin i$  (see Section 3.1.2). We describe how we compare the  $v \sin i$  and rotation period in this section.

The main sample of rotation periods in this work comes from [McQuillan et al. \(2014\)](#). [McQuillan et al. \(2014\)](#) selected their initial sample using the  $T_{\text{eff}}\text{-log}(g)$  cuts advocated by [Ciardi et al. \(2011\)](#) to distinguish between dwarfs and giants. In order to avoid confusion with other periodic signals, [McQuillan et al. \(2014\)](#) removed known eclipsing binaries ([Prša et al.](#)

**Table 2.** Validation Sample Overlap

Sample	Total Size	Overlap with APOGEE
McQuillan et al. (2014) Detections	34030	964
McQuillan et al. (2014) Nondetections	99000	1476
Serenelli et al. (2017)	426	393
García et al. (2014)	310	220
El-Badry et al. (2018b)	20142	904
Berger et al. (2018a)	177911	5337

NOTE— Overlap between validation samples and our main APOGEE sample described in Section 2.2.

2011; Slawson et al. 2011), KOIs (Akeson et al. 2013), and imposed a maximum  $T_{\text{eff}}$  of 6500 K to reduce confusion with pulsators. Their sample to be analyzed contained 133,030 stars.

McQuillan et al. (2014) calculated rotation periods using an autocorrelation function (ACF) based method. The result was a list of 34,030 stars with period detections and 99,000 stars without them.

In addition to the McQuillan et al. (2014) periods, we also make use of surface rotation periods derived for a sample of 310 *Kepler* stars showing asteroseismic oscillations (García et al. 2014), 217 of which have been observed with APOGEE. The García et al. (2014) periods provide a larger overlap with the sample of stars with asteroseismically-derived radii (Serenelli et al. 2017) than McQuillan et al. (2014).

### 2.3.2. Transformation to $v_{\text{eq}}$

$v \sin i$  and rotation period are not directly comparable quantities. However, they can be compared by transforming rotation periods to equatorial velocities through the equation:

$$\log v_{\text{eq}} = \log 2\pi R - \log P \quad (1)$$

where  $R$  is the stellar radius, and  $P$  is the rotation period.

This transformation using the stellar radius means that a flat detection limit of  $10 \text{ km s}^{-1}$

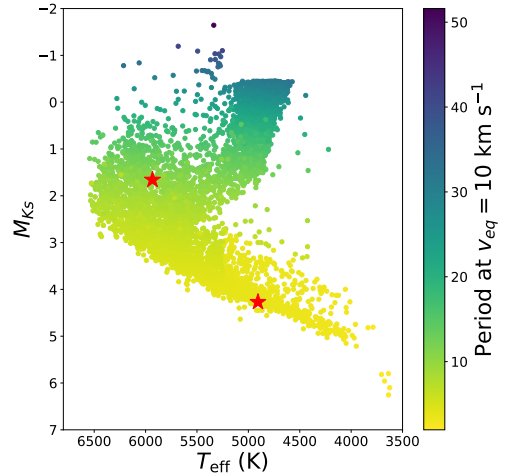


**Figure 3.** HR diagram showing how a detection threshold in velocity translates to period as a function of HR diagram position. The Stefan-Boltzmann radius is used to translate the velocity to a period, except for the cool dwarfs where the deprojected radius is used. Red stars denote the median period threshold in the cool dwarf sample (3.7 days), and in the asteroseismic sample (6.7 days).

(found in Section 3.1.2) translates to a radius-dependent period threshold illustrated in Fig. 3. The period cutoff is 3.7 days for a  $R = 0.74 R_{\odot}$  star, typical of the cool dwarf sample; and 6.7 days for a  $R = 1.3 R_{\odot}$  star, typical of the asteroseismic sample.

The  $\sin i$  ambiguity means that  $v \sin i$  and period are best compared in a statistical sense for large samples. For individual stars, a  $v \sin i$  greater than  $v_{eq}$  implies  $\sin i > 1$ , which is unphysical. However, individual values with  $\sin i \leq 1$  cannot be directly ruled out.

After calculating the equatorial velocity given the period and radius, we construct a distribution by convolving it with a  $\sin i$  distribution, and calculate how much of the convolved distribution remains above the  $v \sin i$  detection limit of  $10 \text{ km s}^{-1}$ . Both period detections and  $v \sin i$  are biased against low  $\sin i$ : spot modulation cannot be seen for low inclination and  $v \sin i$  drops below the instrumental resolution or other broadening mechanisms when the inclination is low enough. Based on prior comparisons in star clusters we truncate our  $\sin i$  convolution kernel at  $\sin i = 0.5$  (Krishnamurthi et al. 1997; Jackson & Jeffries 2010) to correct for this shared bias. We can then compare the observed spectroscopic rapid rotator fraction to that predicted by the photometric rapid rotator fraction in selected populations to serve as an external consistency check between the two measures of rotation. We use this average property, as opposed to a star by star measurement, because it incorporates the known statistical properties of  $\sin i$ . When calculating the spectroscopic rapid rotator fraction we do not include visual SB2s, their  $v \sin i$  will be spuriously overestimated.

### 2.3.3. Binarity

To evaluate our method of identifying binarity in Section 2.1.2, we compare the SB2s derived this way to those determined by El-Badry et al. (2018b). El-Badry et al. (2018b) ran a machine-learning algorithm to flag stars with spectra inconsistent with a single star model. For stars with poor single-star fits, El-Badry et al. (2018b) attempted to find a better-fitting model including a binary companion. El-Badry et al. (2018b) ran their analysis on the APOGEE DR13 release, which only contained 17% of the

Kepler dwarfs and subgiants in DR14, necessitating the visual inspection previously discussed.

When tested in the overlap sample of 308 targets, the El-Badry et al. (2018b) methodology flags visual SB2s exceedingly well. Of the 36 overlap stars visually classified as SB2s, none were classified by El-Badry et al. (2018b) as single stars, suggesting that the El-Badry et al. (2018b) algorithm is complete. In the remaining sample, El-Badry et al. (2018b) flagged an additional 60 stars as SB2s, which is consistent with their method being more sensitive to fainter secondary stars than a visual inspection.

In addition to flagging binaries, El-Badry et al. (2018b) also provide separate stellar parameter estimates for the primary and secondary. We use these stellar parameters in Section 3.1.3 to illustrate the bias imposed by stellar companions on APOGEE stellar parameters, which can be significant.

The results of the comparison show both that the methodology of El-Badry et al. (2018b) is extremely reliable at detecting double-lined spectroscopic binaries, and that the visual SB2 identification does not detect a substantial population of false positives. Unfortunately, because DR14 added many new observations of dwarfs and subgiants which were not in DR13, the El-Badry et al. (2018b) sample is not useful for flagging the majority of SB2s in our sample. Without a comprehensive, reliable method of flagging SB2s, we fall back on identifying SB2s by eye, and assume that the sample of SB2s which are detectable by El-Badry et al. (2018b) but without visible distortion to the spectra will not have dramatically biased stellar parameters.

### 2.3.4. Temperatures

In comparisons using the full McQuillan et al. (2014) sample, most of which do not have APOGEE spectroscopic temperatures, we use the Berger et al. (2018b) photometric temperatures, which are available for nearly the entire

*Kepler* sample, and are based on the fundamental infrared flux method, the same system as that used for APOGEE.

### 3. THE APOGEE $v \sin i$ SAMPLE

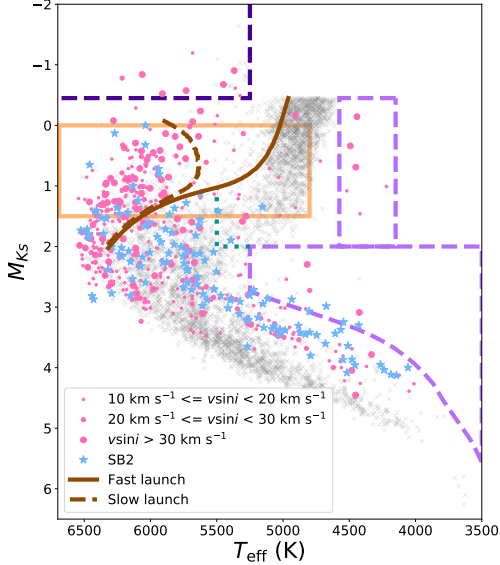


**Figure 4.** Placement of high  $v \sin i$  objects on the HR diagram. The sizes of the marker correspond to bins of  $v \sin i$ . Stars flagged as visual SB2s are light blue stars. Slow rotators are marked as grey crosses. Overplotted are the solar metallicity boundaries predicted by the models in [van Saders & Pinsonneault \(2013\)](#) for the fast and slow launch conditions (solid and dashed brown lines), respectively. These launch conditions represent the initial rotation periods and disk-locking timescales required to match the slowly rotating and rapidly rotating sequences of the Pleiades and M37, respectively. This boundary is quantitatively studied within the orange box in Section 4.1. Also highlighted are blue stragglers (within dashed purple lines), red stragglers and sub-subgiants (within violet lines). The portion of the sample not accessible by the [van Saders & Pinsonneault \(2013\)](#) models is split into regions with high and low rapid rotator fractions (denoted by the aquamarine dotted line).

Our APOGEE sample is illustrated in Fig. 4 (individual rapid rotators highlighted) and

Fig. 5 (rapid rotator fractions indicated). There are striking trends in the distribution of rapid rotators, which can be traced to the influence of two distinct populations. As noted in [Simonian et al. \(2019\)](#), there is a significant rapid rotator background on the photometric binary sequence consistent with a synchronized binary population. Because the *Kepler* fields are old, there is an absence of young, single, rapid rotators. There is also a substantial population of spectroscopic rapid rotators among hotter stars, reflecting the Kraft break between rapid rotation in massive stars and slow rotation in low mass stars. Stars slow down from angular momentum conservation as they cross the subgiant branch, but magnetized winds can be a significant braking mechanism as well. The region where rapid rotation in subgiants is expected from spindown models (brown; described in Section 4.1) is also plotted, in the sense that rapid rotation for a reasonable range of main sequence rotation rates should be confined to the left side of the indicated boundaries. The correspondence between the two is encouraging. We also note the presence of rapid rotation among the red stragglers (stars to the right of the red giant Hayashi track) and the sub-subgiants (stars between the unevolved lower main sequence and the subgiants). These objects appear in star clusters, typically as highly active short period synchronized binaries about to merge ([Geller et al. 2017](#); [Leiner et al. 2017](#)).

In addition to raw counts, the rapid rotator fraction is an interesting population diagnostic. To define the rapid rotator fraction, we bin the HR diagram by luminosity and temperature, and calculate the fraction of targets with  $v \sin i > 10 \text{ km s}^{-1}$  in each bin. The map of rapid rotator fractions is shown in the left panel of Fig. 5

We complement the map of spectroscopic rapid rotator fraction with a map of photometric rapid rotator fraction using the full rotation

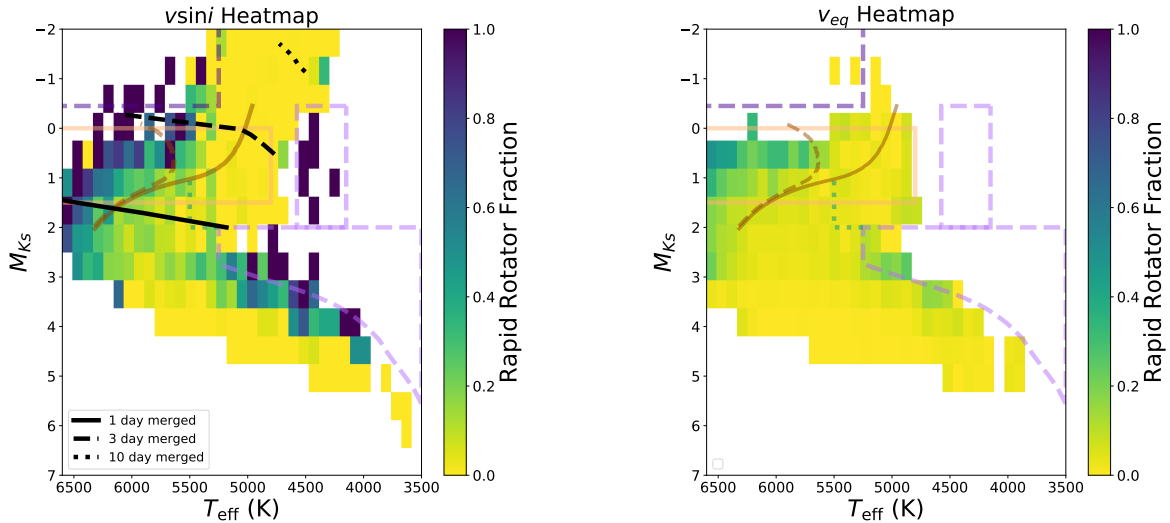


**Figure 5.** *Left:* Map of the rapid rotator fraction in the HR diagram for the APOGEE sample using a threshold of  $v \sin i = 10 \text{ km s}^{-1}$ . The boundaries from Fig. 4 are also reproduced. Black lines mark locations on the HR diagram where binaries on circular orbits with orbital periods of 1 (solid), 3 (dashed), and 10 (dotted) days would undergo Roche-lobe overflow. *Right:* Map of photometric rapid rotator fraction for the full McQuillan et al. (2014) sample with a  $v_{eq} = 10 \text{ km s}^{-1}$  threshold transformed to a period cutoff based on the HR diagram position. Because of the much larger size of the McQuillan et al. (2014) sample, only bins with more than 10 objects are shown. When calculating the rapid rotator fraction, targets which did not have a significant period detection were counted as inactive, slow rotators. van Saders & Pinsonneault (2013) model predictions are the same as on the left.

period sample analyzed by McQuillan et al. (2014) in the right panel of Fig. 5. As we lack APOGEE spectra for most of the McQuillan et al. (2014) targets, we used the photometric temperatures from Berger et al. (2018b), and the same procedure for converting HR diagram position into radius and  $v_{eq}$  as for our main sample. In this diagram we plot the detected rapid rotator fraction, which is the number of stars rotating more rapidly than the radius-dependent threshold corresponding to  $v_{eq} > 10 \text{ km s}^{-1}$  (see Section 2.3.2) divided by the total number of objects in the bin analyzed by McQuillan et al. (2014) whether or not a period was detected. Under the assumption that stars with period nondetections are slow and inactive, this number approximates the true rapid rotator fraction. For hot stars even rapid rotation can produce few spots, so we expect a smaller detection fraction for them.

Through comparing the rapid rotator fraction in McQuillan et al. (2014), we find that in both the subgiant and photometric binary populations the spectroscopic rapid rotator fraction is higher than the photometric rapid rotator fraction. This difference can be readily explained by the fact that rapidly rotating stars with radiative envelopes should not produce spots. However, the difference in the cool rapid rotators is troubling because the McQuillan et al. (2014) sample should be very complete there. We explore the origin of this difference in the sample selection section below.

### 3.1. Sample Validation

From prior work (Tayar et al. 2015) we know that the APOGEE can reliably measure  $v \sin i$  for evolved stars, and the pattern that we see in the hot subgiants in our spectroscopic sample appears reasonable. The photometric rapid

rotator fraction is also in accord with that derived from independent tests on the lower main sequence (Simonian et al. 2019). However, as seen in Fig. 5, our spectroscopic rapid rotator fraction is implausibly large relative to the photometric one for the lower main sequence because one would expect the  $\sin i$  ambiguity to decrease the spectroscopic rapid rotation fraction relative to the photometric rapid rotator fraction rather than the other way around. This indicates a possible background signal that is erroneously interpreted as a  $v \sin i$  in some cases. We therefore employ a series of independent tests of the APOGEE  $v \sin i$  values to understand the source of this background:

1. **Asteroseismic subgiants** We have precise radii from asteroseismic subgiants, making them ideal for testing the concordance between  $v \sin i$  and rotation period in the transition zone between the giant branch and the upper main sequence.
2. **The Pleiades** There is extensive APOGEE spectroscopy in the Pleiades star cluster, where there are both numerous rapid rotators and large independent data sets. This tests the APOGEE data across the FGK main sequence domain.
3. **Rotation Periods on the Lower Main Sequence** We can compare the rotation periods and  $v \sin i$  values directly in the lower main sequence, where we can easily distinguish photometric binaries from single stars without the confounding factor of age effects.

As described in our validation below, we conclude that the APOGEE  $v \sin i$  reliably trace rapid rotation in the subgiant domain, and the discrepancy in the rapid rotator fractions there is caused by reduced spot visibility for hot stars. However, we also find that 13% of photometric binaries in the *Kepler* field have  $v \sin i$  and

rotation period that disagree by at least  $3\sigma$ . We propose that these disagreements have two sources: one from radius inflation of K and M dwarfs, and the other being the presence of unresolved spectrally-blended binaries. Because of these complex systematics, we do not attempt to infer astrophysical properties from samples near the photometric binary sequence, but restrict our main science results in Section 4 to the subgiants.

### 3.1.1. Subgiants with Asteroseismic Data

We begin our validation using *Kepler* targets with both asteroseismic radii and rotation periods. We adopt a  $10 \text{ km s}^{-1}$  threshold for calling stars rapid rotators, derived from the Pleiades test below in Section 3.1.2.

For the asteroseismic sample, we use rotation periods from García et al. (2014) rather than McQuillan et al. (2014) because of the greater overlap. Comparisons using the overlap sample between McQuillan et al. (2014) and García et al. (2014) show that the results are consistent to within their errors, and repeating the following analysis using the smaller overlap sample with McQuillan et al. (2014) yields similar conclusions.

Of the 241 asteroseismic dwarfs with García et al. (2014) rotation periods, 75 have either  $v \sin i > 10 \text{ km s}^{-1}$  or projected equatorial velocities greater than  $10 \text{ km s}^{-1}$ . There were also 21 stars which were classified by Serenelli et al. (2017) as dwarfs, but for which a  $v \sin i$  wasn't calculated by ASPCAP because the spectrum was run with the giant grid. 19 of these stars have equatorial velocities below APOGEE's detection limit, while one has an equatorial velocity of  $12 \text{ km s}^{-1}$ . The final star (KIC 11558953) has an equatorial velocity of  $144 \text{ km s}^{-1}$ , yet no visual signature of broadening in the APOGEE spectrum. This target has a rotation period of 1.01 days, which is on the edge of the 1–100 day grid which García et al. (2014) performed their period search, indicating that this

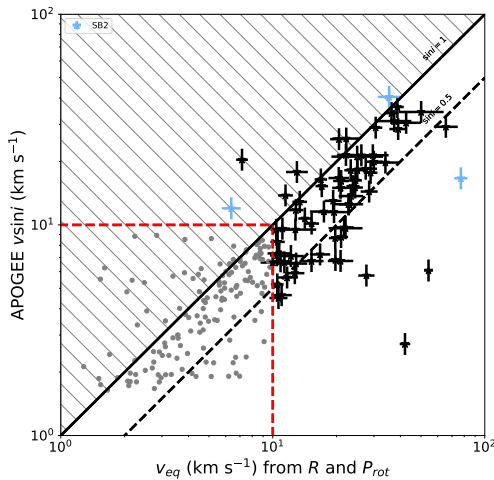


**Figure 6.** Measured  $v \sin i$  compared to the equatorial velocity predicted from rotation period and stellar radius for the asteroseismic sample with García et al. (2014) rotation periods. Targets above either the  $10 \text{ km s}^{-1}$   $v \sin i$  or  $v_{eq}$  detection thresholds (shown as dashed red lines) are denoted as bold points. Targets below both thresholds are de-emphasized for clarity. Not shown are the 21 stars classified by Serenelli et al. (2017) as dwarfs, but with spectra classified by ASPCAP as giant spectra. Blue stars correspond to visually-classified SB2s. The black solid and dashed lines correspond to  $\sin i = 1$  and  $\sin i = 0.5$ , respectively. The hatched region corresponds to  $\sin i > 1$ , which represents an unphysical region.

may be a spurious rotation period. Because the overwhelming majority of targets in the García et al. (2014) overlap sample without  $v \sin i$  are expected to have non-detectable rotation, we classify them all as slow rotators.

The correspondence between the expected and observed velocities for the objects with  $v \sin i$  detections is shown in Fig. 6. The agreement is generally good, with the single notable outlier (KIC 9908400) being a clearly blended source in high-resolution imaging; the rotation signal may not be from the spectroscopic target. There are also three asteroseismic stars (KIC 8656341, KIC 10794845, KIC 10081026) with very low  $\sin i$ , where even accounting for APOGEE’s

$v \sin i$  detection threshold  $\sin i < 0.5$ . KIC 10794845 has clear contamination in the pixel, possibly explaining the two sets of  $v \sin i$  measurements. The other two may be erroneous due to aliasing.

The spectroscopic rapid rotator fraction for the asteroseismic sample is  $19 \pm 3\%$  with a predicted spectroscopic rapid rotator fraction of  $26 \pm 3\%$  after correcting for inclination effects, which are consistent just below the  $2\sigma$  level. If we remove our assumption that  $\sin i > 0.5$ , this discrepancy drops to  $1\sigma$ , which leads us to conclude from the asteroseismic subgiant sample that rotation characteristics of a large sample are robust, even though there may be a few individual outliers.

### 3.1.2. Pleiades Dwarfs with $v \sin i$

While an ideal validation sample would have rapidly-rotating stars representative of the *Kepler* dwarfs, there are not other field star spectroscopic data sets with high enough overlap with APOGEE to be useful. However, the APOGEE survey obtained a large number of spectra in the Pleiades star cluster, which has been the subject of extensive rotational velocity surveys (Stauffer & Hartmann 1987; Queloz et al. 1998; Jackson et al. 2018). Because of its youth, rapid rotation is a general phenomenon there. There is also a large data set of literature  $v \sin i$  available, which we adopt to test the APOGEE  $v \sin i$  values for active dwarfs.

We select stars which were observed both in APOGEE as well as in at least one of these previous studies, cross-matching using the master table in Rebull et al. (2016), which yields a total overlap of 245 observations of 144 targets. A detailed breakdown of the overlap with each survey is given in Table 3, and the cross-matched sample is given in Table 4.

To better characterize the Pleiades sample, we supplement the rotation data with 2MASS photometry (Skrutskie et al. 2006), and look up *Gaia* parallaxes by cross-matching the 2MASS

**Table 3.** APOGEE Overlap with Previous Literature

Survey	R	Overlap
Queloz et al. (1998)	30000	91
Stauffer & Hartmann (1987)	40000	63
Jackson et al. (2018)	17000	91
TOTAL		144

NOTE—Total number is much smaller than the sum of surveys because of large overlap between surveys. For surveys which used multiple instruments, the lowest resolution in the study is displayed.

IDs in Rebull et al. (2016) with the *Gaia* external cross-matched catalog (Marrese et al. 2019). All of the targets in Rebull et al. (2016) that were also observed in APOGEE have parallaxes in *Gaia*.

In an initial comparison, we found that the agreement with the literature was excellent for single stars, but that there were some anomalies for binaries. We therefore separate the sample into photometric single and binaries stars, and illustrate their properties separately. We consider objects in the Pleiades to be photometric binaries if they are more than 0.3 mag above the main-sequence locus in  $\Delta K$  vs  $V - K$  as measured by Stauffer et al. (2016). 31 out of the 144 targets in this sample (or 22%) are photometric binaries.

We compare the APOGEE  $v \sin i$  to literature  $v \sin i$  in Fig. 7. We find that in all datasets, there is an apparent increase in the variance between the APOGEE and literature  $v \sin i$  at  $10 \text{ km s}^{-1}$ . We therefore adopt  $10 \text{ km s}^{-1}$  as the minimum value for a robust detection.

We determined the APOGEE uncertainty by modeling the literature and APOGEE observations for the photometric single stars as independent observations with lognormally-distributed errors for the Stauffer & Hartmann

(1987), Queloz et al. (1998), and Jackson et al. (2018) samples. We choose those three samples because there is a large overlap with APOGEE. We used an MCMC routine (Foreman-Mackey et al. 2013) with a likelihood function:

$$L(\{v_{1,i}\}, \{v_{2,i}\} | \{\sigma_{1,i}\}, \sigma_2, \{v_i\}) = \prod_i \mathcal{N}(\log v_{1,i}; \log v_i, \sigma_{1,i}) \times \mathcal{N}(\log v_{2,i}; \log v_i, \sigma_2) \quad (2)$$

where  $\{v_{1,i}\}$ ,  $\{v_{2,i}\}$  and  $\sigma_{1,i}$  are the known literature  $v \sin i$ , APOGEE  $v \sin i$ , and literature  $v \sin i$  error,  $\{v_i\}$  are the unobserved true  $v \sin i$ , and  $\sigma_2$  is the uncertainty we are trying to derive. We adopt flat priors for all  $\{v_i\}$  and  $\sigma_2$  between  $\log_{10}(1)$  and  $\log_{10}(100)$ .

For the three datasets we used for this analysis, the derived fractional uncertainties were  $12.2^{+2.0}_{-1.7}$ ,  $9.5^{+2.1}_{-1.7}$ , and  $13.0^{+2.2}_{-1.9}$ . As a result, we consider a reasonable uncertainty to be 12%, about the order suggested by Tayar et al. (2015) for APOGEE giants.

In the whole sample we find a total of 7 outliers. We identify outliers by calculating a  $\chi^2$  figure of merit between the literature and APOGEE  $v \sin i$  values for all targets with APOGEE  $v \sin i > 10 \text{ km s}^{-1}$ . We flag  $v \sin i$  discrepant by  $3\sigma$  as inconsistent. 4 of the outliers were observed in both Queloz et al. (1998) and Jackson et al. (2018), and in each case the APOGEE value was discrepant with Queloz et al. (1998), a high-resolution survey, and in agreement with Jackson et al. (2018), a medium-resolution survey. When we identify the  $v \sin i$  outliers in the HR diagram (see Fig. 7), we find that six out of seven lie in the photometric binary sequence. The one single outlier is the one which has an APOGEE  $v \sin i$  of  $11 \text{ km s}^{-1}$ , barely above the detection threshold. The overall discrepancy rate is  $7/144 = 5\%$ , and that for photometric binaries is  $6/31 = 19\%$ . The Pleiades data therefore confirms that APOGEE detections for single

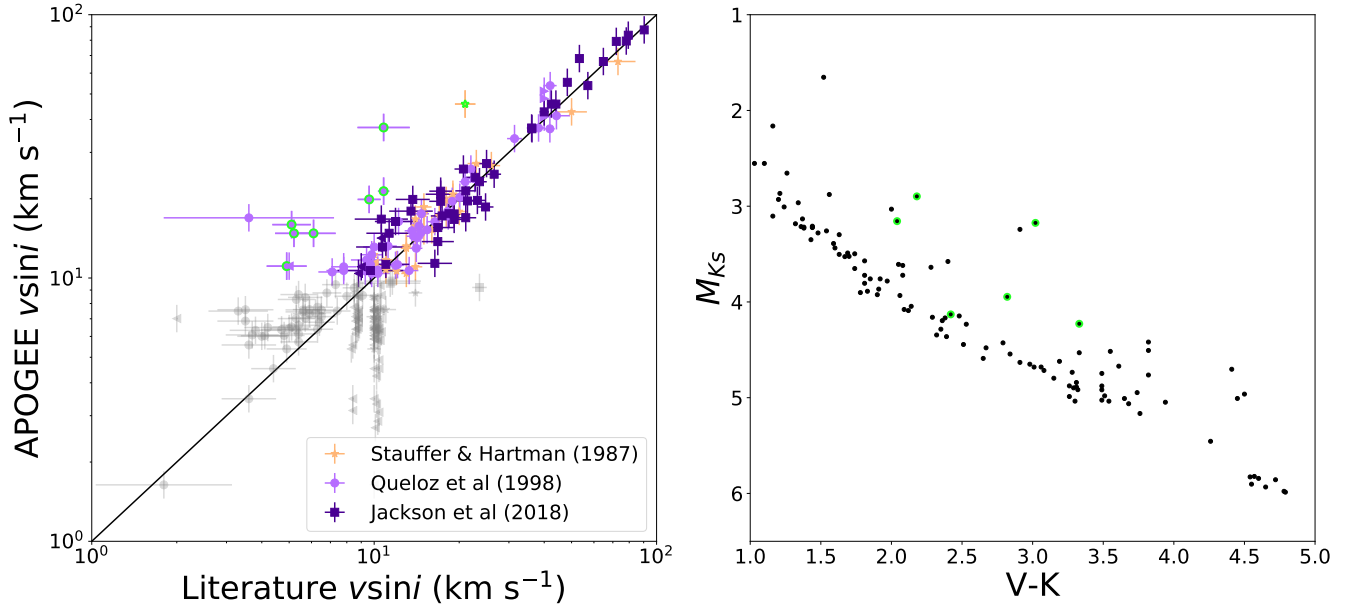


**Figure 7.** *Left:* Comparison of APOGEE  $v \sin i$  to the literature  $v \sin i$  for photometric singles from [Stauffer & Hartmann \(1987\)](#) (orange stars), [Queloz et al. \(1998\)](#) (violet circles), and [Jackson et al. \(2018\)](#) (purple squares). Grey points are below the APOGEE detection limit of 10 km s $^{-1}$ . Left-pointing and right-pointing arrows are reported as lower and upper limits in the original references. 8 outlying observations (for 7 unique targets) are denoted with a green outline. *Right:* The same targets in the  $M_{Ks}$ -(V-K) plane. The 7 targets with outlying observations are denoted with a green outline, and almost all lie on the photometric binary sequence.

stars on the lower main sequence are robust, but that there may be additional systematics for photometric binary stars, which will be more important for field samples.

### 3.1.3. The Unevolved Lower Main Sequence

Having compared directly to literature  $v \sin i$ , we now turn back to the *Kepler* field where we validate against the [McQuillan et al. \(2014\)](#) rotation periods. Because binarity imposes a substantial uncertainty on luminosity-derived radii, we restrict this validation to the unevolved lower main sequence, where photometric binaries can be identified and their excess luminosity corrected for through deprojection. In this sample, we have 512 targets, 151 of which are photometric binaries.

The comparison between the  $v \sin i$  and equatorial velocity for the sample overlapping with [McQuillan et al. \(2014\)](#) is shown in the left panel

of Fig. 8. We mark visual SB2s separately, and they behave as expected; the ASPCAP pipeline attempts to fit the two lines as a single peak and incidentally measures an unphysically high  $v \sin i$ .

However, even when these stars are not considered, there are striking differences between the rapid rotator fractions measured by  $v \sin i$ , and those predicted from a combination of  $R$  and rotation period. The photometric binaries make up 25/27 of the rapid rotators (excluding SB2s), which is consistent with rapid rotation being associated with binaries ([Simonian et al. 2019](#)). However, there is a large disagreement the spectroscopic and photometric rapid rotator fraction. The spectroscopic rapid rotator fraction in the overlap sample is  $8.7^{+2.0}_{-1.7}\%$  while the predicted photometric rapid rotator fraction is  $2.8^{+1.3}_{-0.9}\%$ , a substantial discrepancy.

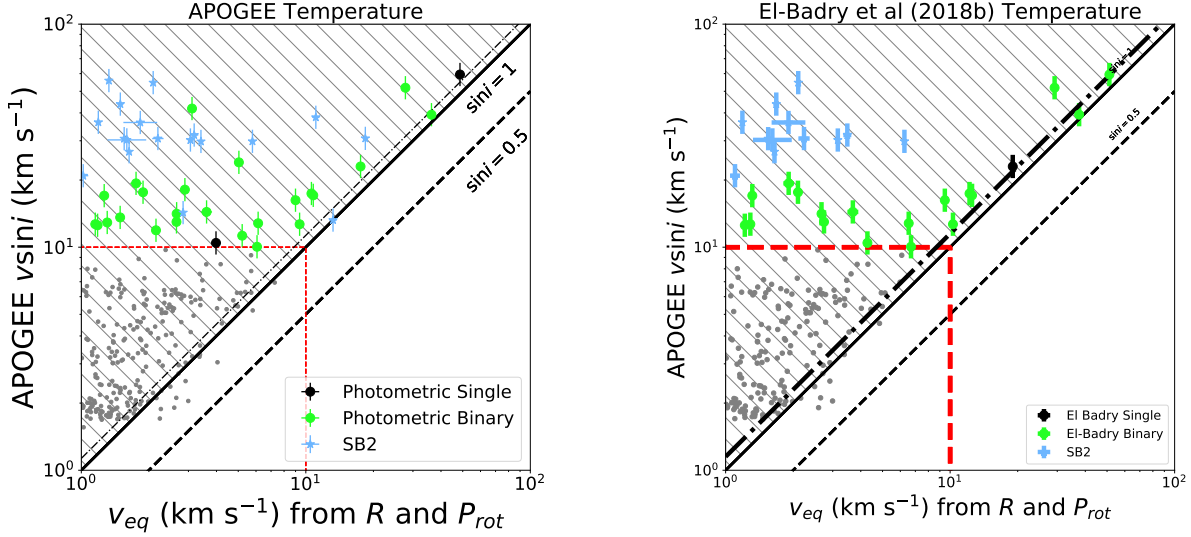


**Figure 8.** *Left:* Same as Fig. 6, with photometric binaries marked in green. The radius is determined by deprojecting targets onto a MIST isochrone. A 13% radius inflation is shown as the dot-dashed line. *Right:* Same as left except for the subset of targets with corrected  $T_{\text{eff}}$  in (El-Badry et al. 2018b). The radius is recalculated using the corrected  $T_{\text{eff}}$ .

Looking at the individual points, 24/27 of the spectroscopic rapid rotators have  $v \sin i$  which is too large given the observed period and radius. These outliers do not show clear signs of contamination as was found for the asteroseismic outlier.

This outlying sample separates into two classes which behave differently. There is a population of stars with high  $v_{\text{eq}}$ , but not as high as that predicted by  $v \sin i$ ; and a slowly rotating population as gauged by  $v_{\text{eq}}$ , but with  $v \sin i$  in the 10 to 15  $\text{km s}^{-1}$  range.

We are comparing  $v \sin i$  to a combination of rotation period and radius; the latter is deduced from the measured  $T_{\text{eff}}$ -R relationship on a standard isochrone. There are therefore three potential error sources: the period, the radius/temperature, or the  $v \sin i$ .

This discrepancy is unlikely to be due to the rotation period. While aliases occur occasionally and may explain points off by a factor of two, the *Kepler* rotation periods have been extensively cross-validated (Aigrain et al. 2015). Additionally, Simonian et al. (2019) found that

the rotation period distribution of the rapid rotators matched the expected orbital period distribution of non-eclipsing binaries inferred from the *Kepler* eclipsing binary sample. Strong systematics in the rotation periods would make this agreement unlikely. We are therefore left with two possibilities: a problem in the radius, or a problem in the  $v \sin i$ .

El-Badry et al. (2018a) found that the APOGEE pipeline could underestimate the  $T_{\text{eff}}$  of photometric binaries, which could produce biased radius estimates. The radius in this regime is determined from the luminosity, bolometric correction, and temperature, all of which depend on the adopted temperature due to the deprojection. To get a sense of the magnitude of this effect, we calculate a radius bias using the subset of stars with corrected temperatures in El-Badry et al. (2018b), which is shown in Fig. 9. The net effect of the temperature underestimation is that the radius is underestimated by a median value of 5.9%. To check if this improves the discrepancy seen in the cool dwarfs, we recompute  $v_{\text{eq}}$  using the revised radius in the

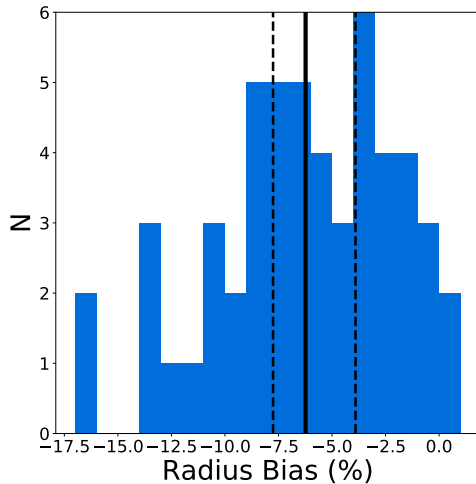


**Figure 9.** The distribution of radius underestimates for the sample of cool dwarfs with decomposed primary  $T_{\text{eff}}$  measurements in [El-Badry et al. \(2018b\)](#). The median underestimation is  $-5.9^{+2.0}_{-1.8}$ , as indicated by the median and  $1\sigma$  percentiles.

right panel of Fig. 8 for the 20 non-SB2 targets. While this does not explain the disagreement for the low  $v_{\text{eq}}$  objects, this correction makes the high  $v_{\text{eq}}$  measurements more plausible.

We use standard isochrones to infer radii, which are known to underpredict the true radii of active K and M stars ([Jackson & Jeffries 2014](#)). Allowing for a radius inflation of 13%, as shown in Fig. 8, can explain the difference for stars which already have high  $v_{\text{eq}}$ , roughly 1/5 of the outliers. A different phenomenon is, however, required to explain the remaining discrepancies.

Evidence that the majority of the high  $v \sin i$  targets represent a background, rather than a true genuine rotation signal, is that most of these stars are either non-detection in [McQuillan et al. \(2014\)](#) or have long measured rotation periods. APOGEE rapid rotators on the lower main sequence would be in a regime where [McQuillan et al. \(2014\)](#) would be very complete, and unlikely to either miss a high-amplitude short period signal or see a low amplitude long period signal instead. Low  $\sin i$  might prevent

detection in starspots, but would also cause low  $v \sin i$ , not high.

We can compare the Pleiades and field star samples to quantify this bias. In the Pleiades,  $19^{+9.8}_{-7.4}\%$  of photometric binaries have discrepant values. In the *Kepler* field, the analogous fraction is  $12.5^{+3.3}_{-2.8}\%$ , so the results from both populations are consistent with each other.

### 3.2. Analysis

The overall reliability of the APOGEE rotation data can be summarized as follows:

1.  $v \sin i$  and rotation periods are concordant for asteroseismic stars.
2.  $v \sin i$  and rotation periods are concordant for stars on the Pleiades single star sequence.
3. 19% of photometric binaries in the Pleiades have  $v \sin i$  which is too high for the rotation period.
4. In all 4 discrepant Pleiades cases with both high- and medium-resolution literature  $v \sin i$  values, the APOGEE  $v \sin i$  agreed with the medium-resolution value, but was discrepant with the high-resolution value.
5. 13% of photometric binaries on the unevolved lower main sequence in the *Kepler* field have  $v \sin i$  which are too high for the rotation period (there are too few rapid rotators on the single-star sequence to draw any meaningful conclusions).
6. Of the *Kepler* rapid rotators with discrepant rotation measures, around 1/5 have both  $v \sin i$  and rotation period above the APOGEE  $v \sin i$  detection threshold, while 4/5 have  $v \sin i$  above the detection threshold, but the rotation period predicts that  $v \sin i$  should be below the detection threshold.

7. The temperature bias predicted by (El-Badry et al. 2018a) is not large enough to explain the discrepancy.
8. Radius inflation can only explain the 1/5 of targets in Item 6.

The combined corrections for radius inflation for rapidly-rotating, active cool stars, and the effect of binarity on radius can resolve the 1/5 of cases, but not for the remaining discrepancies. We instead interpret the anomalously high APOGEE  $v \sin i$  as the APOGEE spectrograph misclassifying unresolved binaries as rapid rotators, which can explain all the trends noted above. This would only occur for binary systems for which the RV offset between the components is comparable to the velocity resolution of the spectrograph ( $\Delta RV = c/\mathcal{R} \sim 14 \text{ km s}^{-1}$ ). This mechanism would predict that there would be a sharp transition in  $v \sin i$  between these spurious spectroscopic rapid rotators and resolved SB2s, which is evident from Fig. 8 at approximately twice the APOGEE resolution. This mechanism would also explain the resolution-dependent discrepancies seen in the Pleiades (see Section 3.1.2), where the low-resolution instruments overestimate the  $v \sin i$  compared to the high-resolution instruments.

This background is most visible in the cool dwarfs because the fraction of spurious rapid rotators  $19/512 = 3.7\%$  is large compared to the fraction of genuine rapid rotators in synchronized binaries, which is around 2% (Simonian et al. 2019). As a result, a 4% background becomes dominant in this regime.

To evaluate the plausibility of this mechanism, we make an order-of-magnitude estimate of how often this phenomenon should be observed in a sample of photometric binaries. We build a toy model of a population of equal-mass  $0.5M_{\odot}$  binaries in circular orbits with a period distribution given by the lognormal distribution in Raghavan et al. (2010). We model the radial

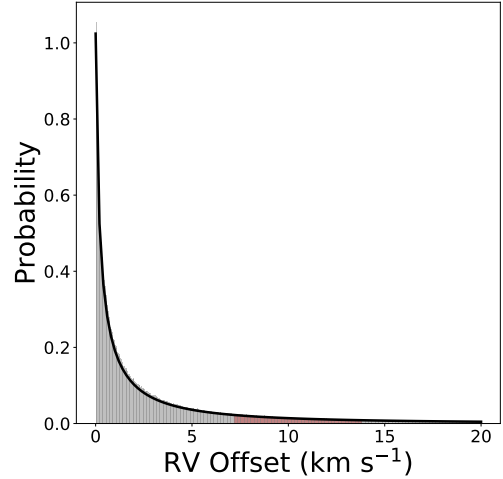


**Figure 10.** Distribution of RV offsets for a population of  $0.5M_{\odot}$  equal-mass binaries in circular orbits following a Raghavan et al. (2010) period distribution. A Monte-carlo realization is shown as the light gray histogram while an analytic expression is shown as the thick black line. The red region denotes the range between  $7 \text{ km s}^{-1} < \Delta v < 14 \text{ km s}^{-1}$ , which is expected to correspond to the case of unresolved spectral blends. Around 10% of the sample falls in between this range.

velocity difference of this population by drawing 1,000,000 randomly distributed periods, inclinations, and orbital phase using Monte Carlo techniques. The histogram along with the analytic estimate is shown in Fig. 10. To estimate the fraction of spectral blends, we assume that all systems where the RV offset is between 0.5–1 times the resolution of the APOGEE spectrograph would correspond to spectral blends, which yields a fraction of 10% in our model photometric binary population. This value is comparable to the fraction that we see in real populations, indicating that this is a plausible explanation for the phenomenon. More detailed modeling, outside of our scope, would be required to quantify and remove this effect from the data set.

## 4. RESULTS

We’ve established that  $v \sin i$  is a reliable tracer of rapid rotation, though it contains a background of spuriously high  $v \sin i$  targets associated with equal-luminosity binaries. To make scientifically interesting conclusions, we seek populations where the signal of genuine rapid rotators is maximized with respect to this background. We argue that the signal-to-background ratio is maximized for the rapidly rotating subgiants.

As seen in Fig. 5, the genuine rapid rotator fraction in the subgiant regime is high. The spectroscopic rapid rotator fraction in the regime hotter than the fast-launch boundary predicted by van Saders & Pinsonneault (2013) is  $17.3^{+1.1}_{-1.0}\%$ , substantially higher than both the fractions expected from spurious binaries and synchronized binaries.

We also expect the background of spectrally blended binaries to decrease for evolved stars because the luminosity contrast between binary components evolves with age. We have three additional pieces of evidence that this effect becomes subdominant among the rapidly-rotating subgiants. First, based on Fig. 5, the rapid rotator fraction clearly increases with luminosity, which is the opposite of what would be expected from a background of near equal-mass binaries. Therefore, this background must be small compared to the single-star rotation signal. Additionally, this effect is not seen in the asteroseismic sample, which is not expected to have a bias against binaries.

Finally, we can see this effect diminish with age in the background-limited regions of the HR diagram. If we remove the notch populated by the rapidly-rotating subgiants, we find that the remaining sample demonstrates a transition (denoted by the aquamarine dotted line in Fig. 4) between a high and low  $v \sin i$  background. The low  $v \sin i$  region (cool and luminous) has a spectroscopic rapid rotator fraction of  $1.2^{+0.4}_{-0.3}\%$ , which is consistent with the tidally-

synchronized background. Based on the contours shown in the left panel of Fig. 5, only a small fraction of the tidally-synchronized population would undergo Roche-lobe overflow and merge. The high  $v \sin i$  region (hot and less luminous) has a rapid rotator fraction of  $5.4^{+0.6}_{-0.5}\%$ , as seen in the cool dwarfs, and is consistent with a 2% synchronized binary population on top of a 4% spectral blend population measured in the cool dwarfs. We conclude that the effect of spectral blends is substantially decreased for evolved stars.

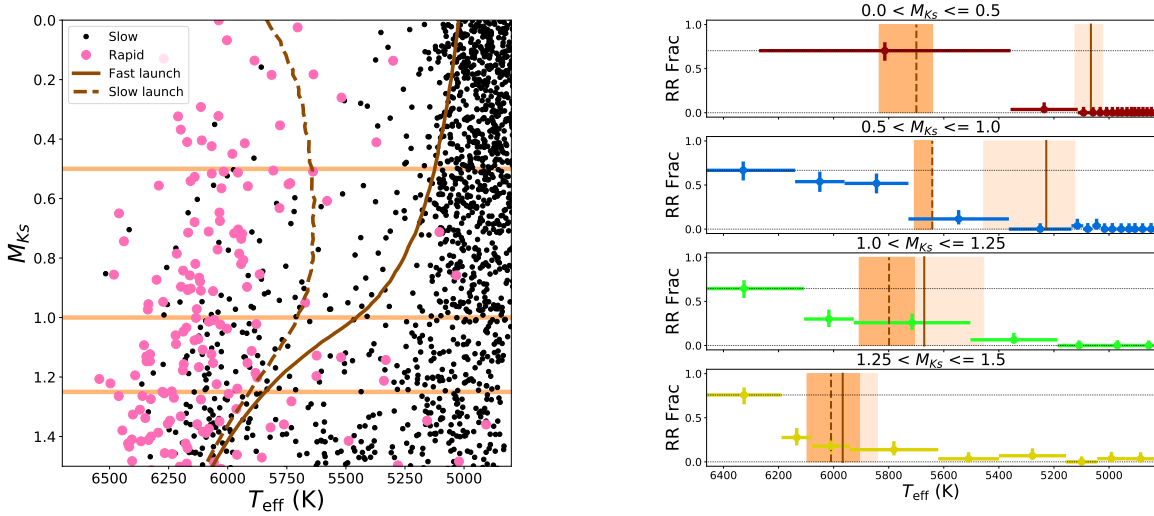
In the sample where  $v \sin i$  is reliable, we note several interesting populations of rapid rotators.

#### 4.1. Subgiant Rotation

We focus our model comparison for hot subgiants between  $2 \geq M_{K_s} > 0$  and  $6500 \text{ K} \geq T_{\text{eff}} > 4900 \text{ K}$  (shown as the orange box in Fig. 4). We leave off the most luminous rapid rotators (delineated by the purple dashed lines in Fig. 11) because this region is too sparsely populated to make meaningful statistical comparisons of  $v \sin i$  to models.

A zoom-in of the main sample is shown in the left panel of Fig. 11. From just the raw data, we see that rapid rotators become more sparse on the cool end. We plot predictions of the boundary separating detectable from undetectable rotation for solar-metallicity stars (van Saders & Pinsonneault 2013). This “iso-velocity” boundary separates hot stars with  $v_{\text{eq}} > 10 \text{ km s}^{-1}$  from cool stars below our detection threshold. The fast and slow launch boundaries correspond to the fast and slow launch conditions described in van Saders & Pinsonneault (2013), and the difference reflects the impact of the range of main sequence rotation rates on the location of the  $v \sin i$  cutoff.

We also note that a similar, albeit subdued trend is seen in the rotation period data in Fig. 4, despite hot subgiants not being expected to have substantial starspots.

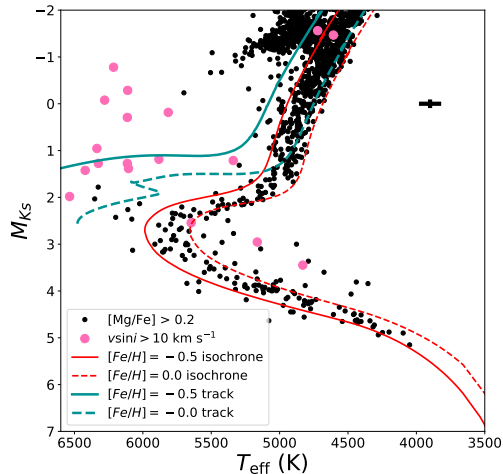


**Figure 11.** *Left:* Rapid rotators emphasized in the zoom-in region denoted in the left panel of Fig. 4. Rapid rotators are denoted as large pink circles while the slow rotators are denoted as black dots. The orange horizontal lines illustrate the luminosity bins for the right figure. The brown lines denote the boundaries predicted by van Saders & Pinsonneault (2013). *Right:* Rapid rotator fraction as a function of  $T_{\text{eff}}$  for four different bins in luminosity. The value of the slow and fast-launch model in the center of each bin is shown as brown vertical lines (dashed and solid). The range of model values within a bin is shown as the shaded region. The maximum and minimum rapid rotator fractions are shown as a horizontal dotted lines.

We perform a rough characterization of the spindown trends in the right panel of Fig. 11, where the rapid rotation fraction with temperature in bins of fixed luminosity is compared to that predicted by the van Saders & Pinsonneault (2013) models. For each luminosity bin, we plot the location of the boundary predicted by van Saders & Pinsonneault (2013) for the slow and fast launch conditions, and the range of the models within each bin. As expected, the detection fraction in the hottest stars is high, reaching a maximum of 68% for all bins; inclination effects and the presence of some very slow rotators on the main sequence can explain why the detection fraction is not 100% to the left of the slow launch boundary. In between the fast and slow launch boundaries, the rapid rotator fraction is expected to drop as the upper envelope continues to decrease and the slower rotators become undetectable. Finally, all stars cooler than the fast launch boundary should have undetectable rotation. The overall pat-

tern is close to that predicted by theory, confirming that the spindown models used for main sequence stars are also viable when applied to hot subgiants evolving to the red giant branch.

In the two least luminous bins, the rapid rotator fraction drops at cooler temperatures than that predicted by models. While this excess of rapid rotators could imply that winds for stars near the Kraft break are overestimated, we note from Fig. 4 that the photometric binary sequence intersects the lowest luminosity bins at  $T_{\text{eff}} \sim 6000$  K. We also note that a corresponding increase in rapid rotators at that position in the HR diagram is not seen in the McQuillan et al. (2014) rotation data. The proximity of this excess to the photometric binary sequence, and its disappearance in the rotation periods leads us to conclude that this discrepancy between the models and the data is likely not be the result of a deficiency in the model, but is rather caused by the high  $v \sin i$  background observed near the photometric binary sequence.

4.2.  $\alpha$ -rich Blue Stragglers

**Figure 12.** The  $\alpha$ -rich APOGEE sample with  $[\text{Mg}/\text{Fe}] > 0.2$ . A representative error bar is shown in the upper right corner. The halo turnoff can be seen in this sample, between two 10 Gyr,  $[\alpha/\text{Fe}] = 0.2$  DSEP isochrones with  $[\text{Fe}/\text{H}] = 0.0$  and  $[\text{Fe}/\text{H}] = -0.5$  (shown in red). DSEP evolutionary tracks for stars representative of the Kraft break ( $1.3M_{\odot}$ ), but with  $[\alpha/\text{Fe}] = 0.2$  and  $[\text{Fe}/\text{H}] = -0.5, 0.0$ , are shown in blue. Stars with  $v \sin i > 10 \text{ km s}^{-1}$  are shown as pink circles.

The *Kepler* field also contains a small population of  $\alpha$ -rich stars, which are generally an old population with a kinematic age of order 10 Gyr (Schuster et al. 2012), well traced by  $[\text{Mg}/\text{Fe}]$  (Hayes et al. 2018). We isolate these stars by imposing a cut of  $[\text{Mg}/\text{Fe}] > 0.2$  and show them in Fig. 12.

In the high  $\alpha$  sequence, we find clear evidence of a turnoff, which we trace between two alpha-enhanced ( $[\alpha/\text{Fe}] = 0.2$ ), 10 Gyr old DSEP isochrones: a high metallicity one with  $[\text{Fe}/\text{H}] = 0.0$ , and a low metallicity one with  $[\text{Fe}/\text{H}] = -0.5$ . The stars hotter than the turnoff are blue stragglers.

Because we define rapid rotation at being at the  $10 \text{ km s}^{-1}$  level or higher, it is likely that all blue stragglers would form as rapid rotators

by our criterion (Sills et al. 2005; Mucciarelli et al. 2014). However, only the stars hotter than the Kraft break would avoid severe spindown from magnetized winds. As a concrete example, Sandquist et al. (2018) found clear evidence for a stellar merger product below the Kraft break on the M67 main sequence that we would count as a slow rotator. At solar metallicity, the Kraft break occurs at  $1.3 M_{\odot}$ , and it is interesting to explore the metallicity dependence of this phenomenon. So we compare the location of the break in the high- $\alpha$  sample to that corresponding to  $\alpha$ -enhanced  $1.3 M_{\odot}$  DSEP evolutionary tracks at high and low metallicity in Fig. 12. We find that the transition between rapid and slow rotators occurs about half-way in between these two tracks, suggesting that the mass of stars at the Kraft break does not change dramatically between solar abundance and this high- $\alpha$  sample.

## 4.3. Red Stragglers

Geller et al. (2017) consolidated stars in numerous clusters which were redder than the single-star isochrone and proposed a standardized nomenclature for them, which we adopt here. “Red Stragglers” are defined as stars more luminous than the turnoff which are substantially redder than the giant branch; “Sub-subgiants” are less luminous than the turnoff and redder than the main sequence, placing them in between the main sequence and the subgiant branch (see Fig. 1 in Geller et al. (2017)). While the turnoff is not as well defined for a field population as it is in a cluster, we find likely analogs of red stragglers and sub-subgiants in the APOGEE field population.

Both red stragglers and sub-subgiants occupy regions of the HR diagram which are not accessible to single-star evolution, and are believed to involve multi-star interactions. The three most promising explanations are that the red stragglers are: (1) mass-transfer systems out of thermodynamic equilibrium, (2) stripped subgiants

from close encounters, and (3) underluminous, magnetically active subgiants in a synchronized binary (Leiner et al. 2017). All three mechanisms would leave a signature of rapid rotation as a result of the stellar interaction, which we see in the APOGEE data.

In the red stragglers, we find definite signatures of rapid rotation. Of the 7 red stragglers in our sample, 6 have  $v \sin i > 10 \text{ km s}^{-1}$ , which is consistent with a fully rapidly-rotating population. Of this sample, 3 have been observed by APOGEE over multiple epochs, and all show RV variability greater than  $30 \text{ km s}^{-1}$ , demonstrating that they are likely close binaries. One red straggler has a rotation period of 10.8 days, which is consistent with its radius and  $v \sin i$ , and also consistent with estimates of the synchronization threshold on the main sequence (Mazeh 2008). These systems are extremely prominent in the HR diagram, and are likely an interesting population to study in the field with APOGEE.

Of the 28 stars in the sub-subgiant region, only a few appear to be true sub-subgiants. 6 of them are visual SB2s, which we exclude because their stellar properties are likely unreliable. 7 of the remaining sample have  $v \sin i > 10 \text{ km s}^{-1}$  including 2 lower limits, implying a rapid rotation fraction of 32%. Two of the spectroscopic rapid rotators have rotation periods in McQuillan et al. (2014). One has a 23 day period which is too long for its  $v \sin i$ , demonstrating the presence of spectral blends in this sample. The other has a 0.3 day period and an upper limit of  $v \sin i > 87 \text{ km s}^{-1}$ , implying it's a genuine rapid rotator. However, it does not have detectable RV variability, which means it may not have a close binary companion, and would be an interesting target for further study. We conclude that while this regime does contain a genuine sample of rapid rotators, biased stellar parameters caused by binarity can also spuriously populate this region. We suggest that

special care be taken to study these targets in detail with specifically chosen methods that are robust to binarity.

## 5. DISCUSSION AND CONCLUSION

We validated the catalog  $v \sin i$  for a sample of 5,337 dwarfs and subgiants observed by APOGEE by comparing against Kepler rotation periods and literature  $v \sin i$ . In this sample, we found:

- Moderate-resolution spectroscopy produces a spuriously high  $v \sin i$  background caused by spectral blending of binaries at the level of 4% of the population.
- This background is less common for evolved populations. It can be negligible for intrinsically rapidly rotating populations such as the subgiants, for which we found agreement with the models of van Saders & Pinsonneault (2013).
- The location of the Kraft break for a high- $\alpha$  population is consistent with that expected based on the solar-metallicity population.
- APOGEE can detect rapid rotation for exotic classes of synchronized binaries such as sub-subgiants and red stragglers.

Huber et al. (2014) enlarged the sample of stars with KIC parameters by using 2MASS data for objects without *griz* photometry. The agreement between their properties and those in APOGEE is reasonable (see Appendix A for details), but we caution that the agreement between the photometric and spectroscopic data is degraded relative to the performance in the sample with *griz* data.

In the age of large datasets, binarity needs to be adequately corrected for in order to measure the effects of rare populations. With the advent of *Gaia* parallaxes, luminosity information is widely available as a useful tool to separate single stars from photometric binaries. For

analyses focusing on single stars, removing the photometric binaries can be a useful step in ensuring a well-behaved sample despite the fact that it will remove genuine hot evolved stars. Modeling is another technique to account for the effects of binaries. However, it is complicated by the fact that the binary population is highly sensitive to how the sample was selected. For example, binaries will be overrepresented in magnitude-limited samples (Simonian et al. 2019) so their impact on the population will necessarily change depending on the sample.

We touched upon the largely unstudied role of metallicity on rotation in the high- $\alpha$  sample, and explore metallicity more fully by binning the sample by metallicity in Fig. 13 with the corresponding metallicity-adjusted van Saders & Pinsonneault (2013) models. There are qualitative differences in the behavior of the model and the data, but our sample does not have enough metal-rich and metal-poor stars to meaningfully constrain the behavior of the models. One way to increase the number of high and low-metallicity targets is to expand the sample beyond the *Kepler* field, which can be used to further constrain the behavior of rotation with metallicity.

Investigations into metallicity trends with rotation need to be wary of trends in binarity with metallicity. Recent results have shown that the field binary fraction may be anticorrelated with metallicity (El-Badry & Rix 2019; Moe et al. 2019). These results are in agreement with what we observe in the *Kepler* field, shown in Fig. 13. The metal-poor regime contains a large fraction of photometric binaries (hence high- $v_{\text{sin}i}$  stars), while the metal-rich regime is nearly devoid of photometric binaries. Investigations into how a population which contains binaries changes with metallicity will need to control for these effects.

G.S, M.P. and D.T acknowledge support from NASA ADP Grant NNX15AF13G and from the National Science Foundation via grant AST-1411685 to The Ohio State University. G.S. is also grateful to Jamie Tayar for illuminating conversations regarding the APOKASC catalog as well as stellar rotation in general. We also thank the anonymous referee for their highly clarifying suggestions.

*Facility:* Kepler, Gaia, CTIO:2MASS, Sloan

*Software:* MIST (Choi et al. 2016), Astropy (Astropy Collaboration et al. 2013), IPython (Pérez & Granger 2007), Scipy (jon 2001), NumPy (Van Der Walt et al. 2011), Matplotlib (Hunter 2007)

## REFERENCES

- 2001, SciPy: Open source scientific tools for Python. <http://www.scipy.org/>
- Abolfathi, B., Aguado, D. S., Aguilar, G., et al. 2018, *ApJS*, 235, 42, doi: [10.3847/1538-4365/aa9e8a](https://doi.org/10.3847/1538-4365/aa9e8a)
- Aigrain, S., Llama, J., Ceillier, T., et al. 2015, *MNRAS*, 450, 3211, doi: [10.1093/mnras/stv853](https://doi.org/10.1093/mnras/stv853)
- Akeson, R. L., Chen, X., Ciardi, D., et al. 2013, *PASP*, 125, 989, doi: [10.1086/672273](https://doi.org/10.1086/672273)
- Allende Prieto, C., Beers, T. C., Wilhelm, R., et al. 2006, *ApJ*, 636, 804, doi: [10.1086/498131](https://doi.org/10.1086/498131)
- Angus, R., Aigrain, S., Foreman-Mackey, D., & McQuillan, A. 2015, *MNRAS*, 450, 1787, doi: [10.1093/mnras/stv423](https://doi.org/10.1093/mnras/stv423)
- Astropy Collaboration, Robitaille, T. P., Tollerud, E. J., et al. 2013, *A&A*, 558, A33, doi: [10.1051/0004-6361/201322068](https://doi.org/10.1051/0004-6361/201322068)
- Attridge, J. M., & Herbst, W. 1992, *ApJL*, 398, L61, doi: [10.1086/186577](https://doi.org/10.1086/186577)
- Barnes, S. A. 2007, *ApJ*, 669, 1167, doi: [10.1086/519295](https://doi.org/10.1086/519295)
- Berger, T. A., Howard, A. W., & Boesgaard, A. M. 2018a, *ApJ*, 855, 115, doi: [10.3847/1538-4357/aab154](https://doi.org/10.3847/1538-4357/aab154)

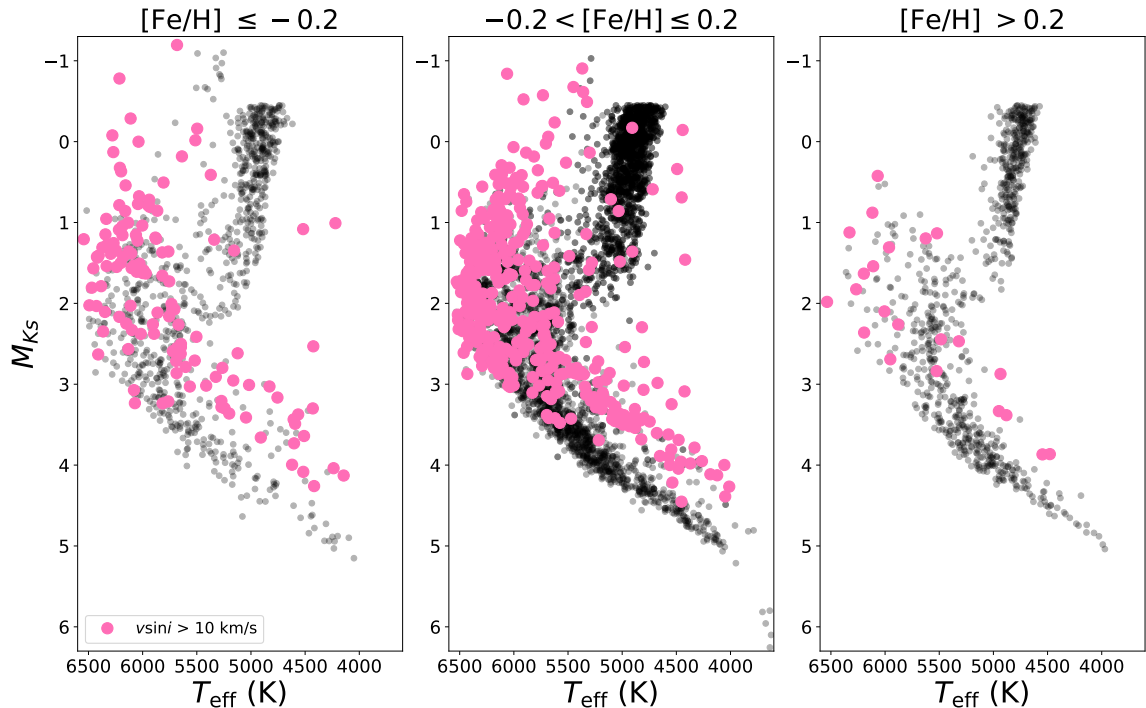


**Figure 13.** Rapid Rotators highlighted for three bins of metallicity with boundaries of  $[\text{Fe}/\text{H}] = -0.2, 0.0, 0.2$ . Rapid rotators are emphasized as pink circles.

- Berger, T. A., Huber, D., Gaidos, E., & van Saders, J. L. 2018b, *ApJ*, 866, 99, doi: [10.3847/1538-4357/aada83](https://doi.org/10.3847/1538-4357/aada83)
- Brown, T. M., Latham, D. W., Everett, M. E., & Esquerdo, G. A. 2011, *AJ*, 142, 112, doi: [10.1088/0004-6256/142/4/112](https://doi.org/10.1088/0004-6256/142/4/112)
- Cardelli, J. A., Clayton, G. C., & Mathis, J. S. 1989, *ApJ*, 345, 245, doi: [10.1086/167900](https://doi.org/10.1086/167900)
- Chaplin, W. J., Kjeldsen, H., Christensen-Dalsgaard, J., et al. 2011, *Science*, 332, 213, doi: [10.1126/science.1201827](https://doi.org/10.1126/science.1201827)
- Choi, J., Dotter, A., Conroy, C., et al. 2016, *ApJ*, 823, 102, doi: [10.3847/0004-637X/823/2/102](https://doi.org/10.3847/0004-637X/823/2/102)
- Ciardi, D. R., von Braun, K., Bryden, G., et al. 2011, *AJ*, 141, 108, doi: [10.1088/0004-6256/141/4/108](https://doi.org/10.1088/0004-6256/141/4/108)
- Deheuvels, S., Doğan, G., Goupil, M. J., et al. 2014, *A&A*, 564, A27, doi: [10.1051/0004-6361/201322779](https://doi.org/10.1051/0004-6361/201322779)
- El-Badry, K., & Rix, H.-W. 2019, *MNRAS*, 482, L139, doi: [10.1093/mnras/sly206](https://doi.org/10.1093/mnras/sly206)
- El-Badry, K., Rix, H.-W., Ting, Y.-S., et al. 2018a, *MNRAS*, 473, 5043, doi: [10.1093/mnras/stx2758](https://doi.org/10.1093/mnras/stx2758)
- El-Badry, K., Ting, Y.-S., Rix, H.-W., et al. 2018b, *MNRAS*, 476, 528, doi: [10.1093/mnras/sty240](https://doi.org/10.1093/mnras/sty240)
- Foreman-Mackey, D., Hogg, D. W., Lang, D., & Goodman, J. 2013, *PASP*, 125, 306, doi: [10.1086/670067](https://doi.org/10.1086/670067)
- Gaia Collaboration, Brown, A. G. A., Vallenari, A., et al. 2018, *A&A*, 616, A1, doi: [10.1051/0004-6361/201833051](https://doi.org/10.1051/0004-6361/201833051)
- García, R. A., Ceillier, T., Salabert, D., et al. 2014, *A&A*, 572, A34, doi: [10.1051/0004-6361/201423888](https://doi.org/10.1051/0004-6361/201423888)
- García Pérez, A. E., Allende Prieto, C., Holtzman, J. A., et al. 2016, *AJ*, 151, 144, doi: [10.3847/0004-6256/151/6/144](https://doi.org/10.3847/0004-6256/151/6/144)
- Gehan, C., Mosser, B., Michel, E., Samadi, R., & Kallinger, T. 2018, *A&A*, 616, A24, doi: [10.1051/0004-6361/201832822](https://doi.org/10.1051/0004-6361/201832822)
- Geller, A. M., Leiner, E. M., Bellini, A., et al. 2017, *ApJ*, 840, 66, doi: [10.3847/1538-4357/aa6af3](https://doi.org/10.3847/1538-4357/aa6af3)
- Gilhool, S. H., Blake, C. H., Terrien, R. C., et al. 2018, *AJ*, 155, 38, doi: [10.3847/1538-3881/aa9c7c](https://doi.org/10.3847/1538-3881/aa9c7c)
- González Hernández, J. I., & Bonifacio, P. 2009, *A&A*, 497, 497, doi: [10.1051/0004-6361/200810904](https://doi.org/10.1051/0004-6361/200810904)

- Green, G. M., Schlafly, E. F., Finkbeiner, D., et al. 2018, *MNRAS*, 478, 651, doi: [10.1093/mnras/sty1008](https://doi.org/10.1093/mnras/sty1008)
- Gunn, J. E., Siegmund, W. A., Mannery, E. J., et al. 2006, *AJ*, 131, 2332, doi: [10.1086/500975](https://doi.org/10.1086/500975)
- Hayes, C. R., Majewski, S. R., Shetrone, M., et al. 2018, *ApJ*, 852, 49, doi: [10.3847/1538-4357/aa9cec](https://doi.org/10.3847/1538-4357/aa9cec)
- Henderson, C. B., & Stassun, K. G. 2012, *ApJ*, 747, 51, doi: [10.1088/0004-637X/747/1/51](https://doi.org/10.1088/0004-637X/747/1/51)
- Herbst, W., Maley, J. A., & Williams, E. C. 2000, *AJ*, 120, 349, doi: [10.1086/301430](https://doi.org/10.1086/301430)
- Holtzman, J. A., Hasselquist, S., Shetrone, M., et al. 2018, *AJ*, 156, 125, doi: [10.3847/1538-3881/aad4f9](https://doi.org/10.3847/1538-3881/aad4f9)
- Huber, D., Silva Aguirre, V., Matthews, J. M., et al. 2014, *ApJS*, 211, 2, doi: [10.1088/0067-0049/211/1/2](https://doi.org/10.1088/0067-0049/211/1/2)
- Hunter, J. D. 2007, *Computing In Science & Engineering*, 9, 90
- Jackson, R. J., Deliyannis, C. P., & Jeffries, R. D. 2018, *MNRAS*, doi: [10.1093/mnras/sty374](https://doi.org/10.1093/mnras/sty374)
- Jackson, R. J., & Jeffries, R. D. 2010, *MNRAS*, 402, 1380, doi: [10.1111/j.1365-2966.2009.15983.x](https://doi.org/10.1111/j.1365-2966.2009.15983.x)
- . 2014, *MNRAS*, 445, 4306, doi: [10.1093/mnras/stu2076](https://doi.org/10.1093/mnras/stu2076)
- Kaler, J. B. 1989, *Stars and their spectra. an introduction to spectral sequence*
- Kawaler, S. D. 1988, *ApJ*, 333, 236, doi: [10.1086/166740](https://doi.org/10.1086/166740)
- Kraft, R. P. 1967, *ApJ*, 150, 551, doi: [10.1086/149359](https://doi.org/10.1086/149359)
- Krishnamurthi, A., Pinsonneault, M. H., Barnes, S., & Sofia, S. 1997, *ApJ*, 480, 303, doi: [10.1086/303958](https://doi.org/10.1086/303958)
- Kurucz, R. L. 1970, *SAO Special Report*, 309
- . 1993, *SYNTHE spectrum synthesis programs and line data*
- Leiner, E., Mathieu, R. D., & Geller, A. M. 2017, *ApJ*, 840, 67, doi: [10.3847/1538-4357/aa6aff](https://doi.org/10.3847/1538-4357/aa6aff)
- Luri, X., Brown, A. G. A., Sarro, L. M., et al. 2018, *A&A*, 616, A9, doi: [10.1051/0004-6361/201832964](https://doi.org/10.1051/0004-6361/201832964)
- Majewski, S. R., Schiavon, R. P., Frinchaboy, P. M., et al. 2017, *AJ*, 154, 94, doi: [10.3847/1538-3881/aa784d](https://doi.org/10.3847/1538-3881/aa784d)
- Mamajek, E. E., & Hillenbrand, L. A. 2008, *ApJ*, 687, 1264, doi: [10.1086/591785](https://doi.org/10.1086/591785)
- Marrese, P. M., Marinoni, S., Fabrizio, M., & Altavilla, G. 2019, *A&A*, 621, A144, doi: [10.1051/0004-6361/201834142](https://doi.org/10.1051/0004-6361/201834142)
- Mazeh, T. 2008, in *EAS Publications Series*, ed. M. J. Goupil & J. P. Zahn, Vol. 29, 1–65
- McQuillan, A., Mazeh, T., & Aigrain, S. 2014, *ApJS*, 211, 24, doi: [10.1088/0067-0049/211/2/24](https://doi.org/10.1088/0067-0049/211/2/24)
- Metcalf, T. S., Egeland, R., & van Saders, J. 2016, *ApJL*, 826, L2, doi: [10.3847/2041-8205/826/1/L2](https://doi.org/10.3847/2041-8205/826/1/L2)
- Metcalf, T. S., & van Saders, J. 2017, *SoPh*, 292, 126, doi: [10.1007/s11207-017-1157-5](https://doi.org/10.1007/s11207-017-1157-5)
- Moe, M., & Di Stefano, R. 2017, *ApJS*, 230, 15, doi: [10.3847/1538-4365/aa6fb6](https://doi.org/10.3847/1538-4365/aa6fb6)
- Moe, M., Kratter, K. M., & Badenes, C. 2019, *ApJ*, 875, 61, doi: [10.3847/1538-4357/ab0d88](https://doi.org/10.3847/1538-4357/ab0d88)
- Mosser, B., Goupil, M. J., Belkacem, K., et al. 2012, *A&A*, 548, A10, doi: [10.1051/0004-6361/201220106](https://doi.org/10.1051/0004-6361/201220106)
- Mucciarelli, A., Lovisi, L., Ferraro, F. R., et al. 2014, *ApJ*, 797, 43, doi: [10.1088/0004-637X/797/1/43](https://doi.org/10.1088/0004-637X/797/1/43)
- Netopil, M., Paunzen, E., Heiter, U., & Soubiran, C. 2016, *A&A*, 585, A150, doi: [10.1051/0004-6361/201526370](https://doi.org/10.1051/0004-6361/201526370)
- Parker, E. N. 1958, *ApJ*, 128, 664, doi: [10.1086/146579](https://doi.org/10.1086/146579)
- Pérez, F., & Granger, B. E. 2007, *Computing in Science and Engineering*, 9, 21, doi: [10.1109/MCSE.2007.53](https://doi.org/10.1109/MCSE.2007.53)
- Pinsonneault, M. H., An, D., Molenda-Żakowicz, J., et al. 2012, *ApJS*, 199, 30, doi: [10.1088/0067-0049/199/2/30](https://doi.org/10.1088/0067-0049/199/2/30)
- Prša, A., Batalha, N., Slawson, R. W., et al. 2011, *AJ*, 141, 83, doi: [10.1088/0004-6256/141/3/83](https://doi.org/10.1088/0004-6256/141/3/83)
- Queloz, D., Allain, S., Mermilliod, J. C., Bouvier, J., & Mayor, M. 1998, *A&A*, 335, 183, <https://arxiv.org/abs/astro-ph/9803138>
- Raghavan, D., McAlister, H. A., Henry, T. J., et al. 2010, *ApJS*, 190, 1, doi: [10.1088/0067-0049/190/1/1](https://doi.org/10.1088/0067-0049/190/1/1)
- Rebull, L. M., Stauffer, J. R., Bouvier, J., et al. 2016, *AJ*, 152, 113, doi: [10.3847/0004-6256/152/5/113](https://doi.org/10.3847/0004-6256/152/5/113)
- Sandquist, E. L., Mathieu, R. D., Quinn, S. N., et al. 2018, *AJ*, 155, 152, doi: [10.3847/1538-3881/aab0ff](https://doi.org/10.3847/1538-3881/aab0ff)
- Schuster, W. J., Moreno, E., Nissen, P. E., & Pichardo, B. 2012, *A&A*, 538, A21, doi: [10.1051/0004-6361/201118035](https://doi.org/10.1051/0004-6361/201118035)

- Serenelli, A., Johnson, J., Huber, D., et al. 2017, *ApJS*, 233, 23, doi: [10.3847/1538-4365/aa97df](https://doi.org/10.3847/1538-4365/aa97df)
- Sills, A., Adams, T., & Davies, M. B. 2005, *MNRAS*, 358, 716, doi: [10.1111/j.1365-2966.2005.08809.x](https://doi.org/10.1111/j.1365-2966.2005.08809.x)
- Simonian, G. V. A., Pinsonneault, M. H., & Terndrup, D. M. 2019, *ApJ*, 871, 174, doi: [10.3847/1538-4357/aaf97c](https://doi.org/10.3847/1538-4357/aaf97c)
- Skrutskie, M. F., Cutri, R. M., Stiening, R., et al. 2006, *AJ*, 131, 1163, doi: [10.1086/498708](https://doi.org/10.1086/498708)
- Slawson, R. W., Prša, A., Welsh, W. F., et al. 2011, *AJ*, 142, 160, doi: [10.1088/0004-6256/142/5/160](https://doi.org/10.1088/0004-6256/142/5/160)
- Stauffer, J., Rebull, L., Bouvier, J., et al. 2016, *AJ*, 152, 115, doi: [10.3847/0004-6256/152/5/115](https://doi.org/10.3847/0004-6256/152/5/115)
- Stauffer, J. R., & Hartmann, L. W. 1987, *ApJ*, 318, 337, doi: [10.1086/165371](https://doi.org/10.1086/165371)
- Tayar, J., Ceillier, T., García-Hernández, D. A., et al. 2015, *ApJ*, 807, 82, doi: [10.1088/0004-637X/807/1/82](https://doi.org/10.1088/0004-637X/807/1/82)
- Van Der Walt, S., Colbert, S. C., & Varoquaux, G. 2011, *Computing in Science & Engineering*, 13, 22
- van Saders, J. L., Ceillier, T., Metcalfe, T. S., et al. 2016, *Nature*, 529, 181, doi: [10.1038/nature16168](https://doi.org/10.1038/nature16168)
- van Saders, J. L., & Pinsonneault, M. H. 2013, *ApJ*, 776, 67, doi: [10.1088/0004-637X/776/2/67](https://doi.org/10.1088/0004-637X/776/2/67)
- van Saders, J. L., Pinsonneault, M. H., & Barbieri, M. 2019, *ApJ*, 872, 128, doi: [10.3847/1538-4357/aafafe](https://doi.org/10.3847/1538-4357/aafafe)
- Weber, E. J., & Davis, Jr., L. 1967, *ApJ*, 148, 217, doi: [10.1086/149138](https://doi.org/10.1086/149138)
- Wilson, J. C., Hearty, F., Skrutskie, M. F., et al. 2010, in *Proc. SPIE*, Vol. 7735, *Ground-based and Airborne Instrumentation for Astronomy III*, 77351C
- Zasowski, G., Cohen, R. E., Chojnowski, S. D., et al. 2017, *AJ*, 154, 198, doi: [10.3847/1538-3881/aa8df9](https://doi.org/10.3847/1538-3881/aa8df9)
- Zinn, J. C., Pinsonneault, M. H., Huber, D., & Stello, D. 2019, *ApJ*, 878, 136, doi: [10.3847/1538-4357/ab1f66](https://doi.org/10.3847/1538-4357/ab1f66)

## APPENDIX

## A. HUBER ET AL (2014) TEMPERATURE

One significant benefit of the APOGEE targeting criteria being based on Huber et al. (2014) stellar parameters is that APOGEE independently measured temperatures for stars which previously only had  $T_{\text{eff}}$  and evolutionary state classifications from 2MASS colors. We perform a quick validation of those parameters to determine the reliability of stellar classifications based only on 2MASS photometry.

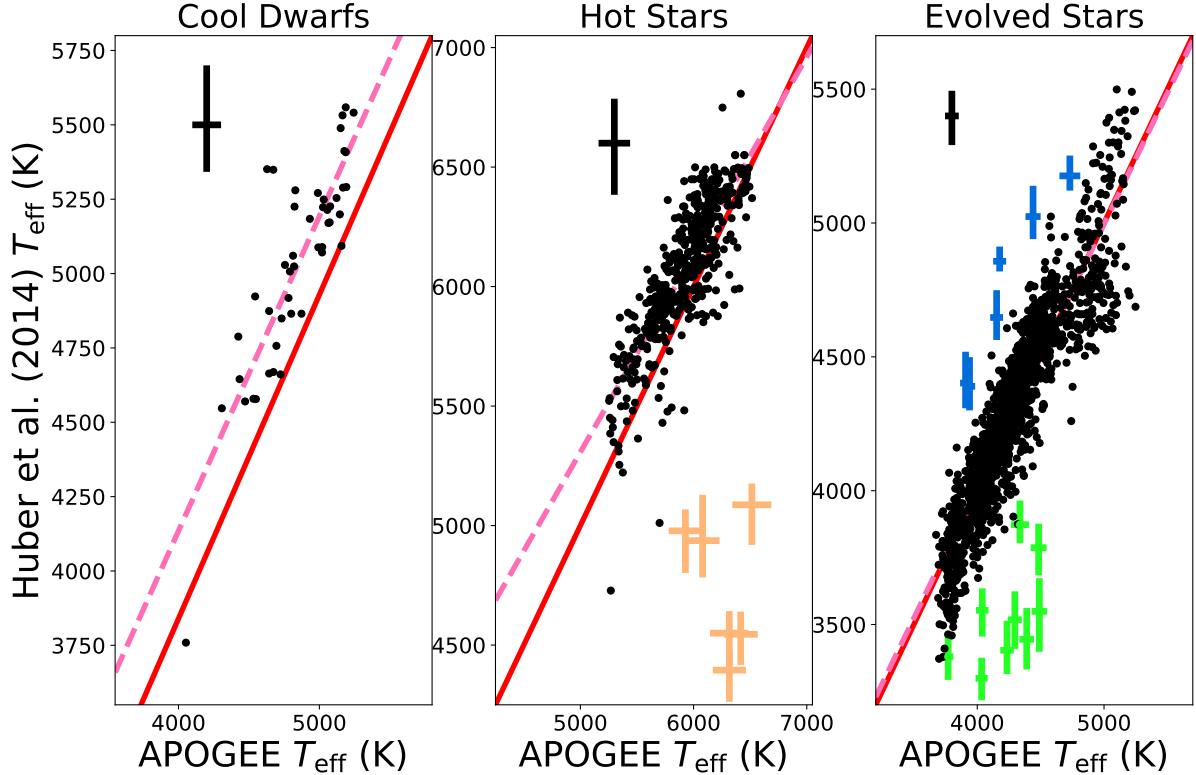


**Figure 14.** *Left:* Comparison between Huber et al. (2014) and APOGEE effective temperatures for cool dwarfs and photometric binaries with temperatures determined from 2MASS photometry and independently measured by APOGEE. A representative error bar for the bulk of the sample is shown in the top left corner. The solid red line denotes the one-to-one relation. The dashed pink line denotes the best linear fit with equation  $T_{\text{eff}}(\text{Huber}) = 1.06T_{\text{eff}}(\text{APOGEE}) - 98$  K with a scatter of 177 K. *Middle:* Same as left, except for the hot star sample. The best-fit relation is given as  $T_{\text{eff}}(\text{Huber}) = 0.83T_{\text{eff}}(\text{APOGEE}) - 1173$  K with an RMS scatter of 159 K. Points with APOGEE  $T_{\text{eff}}$  more than  $4\sigma$  higher than the one-to-one relation are marked as orange points, and were excluded from the fit and scatter. *Right:* Same as left, except for the evolved stars. The best-fit relation in this regime is given as  $T_{\text{eff}}(\text{Huber}) = 0.98T_{\text{eff}}(\text{APOGEE}) - 91$  K with a scatter of 142 K. Points with APOGEE  $T_{\text{eff}}$  more than  $4\sigma$  greater than the one-to-one line are marked in green, while points with APOGEE  $T_{\text{eff}}$  more than  $4\sigma$  lower than the one-to-one line are marked in blue. Both sets of outliers were excluded from the fit and scatter.

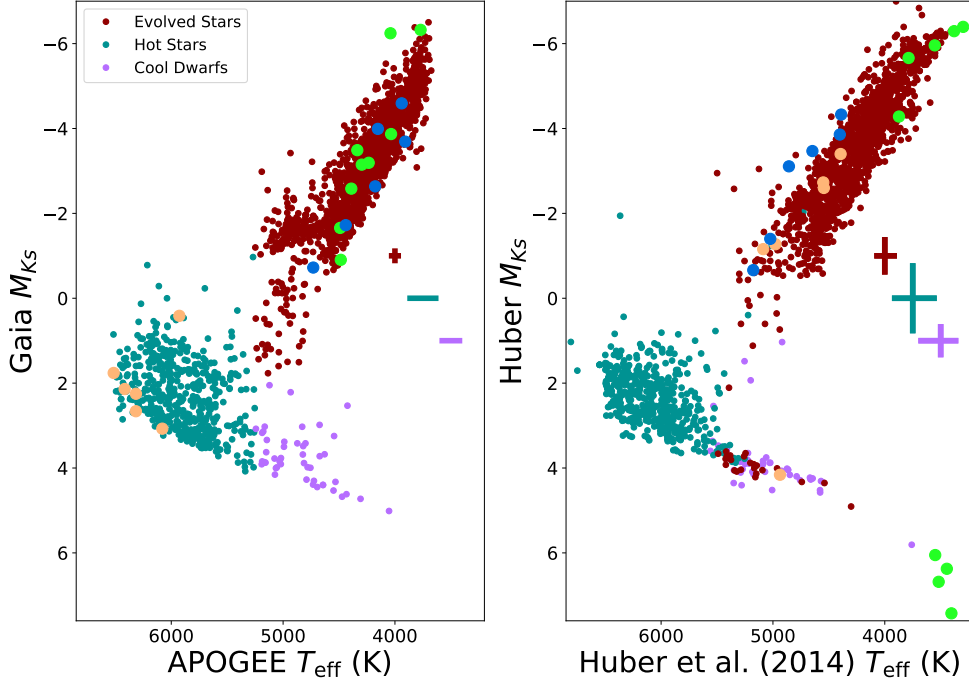


**Figure 15.** *Left:* Standard evolutionary state classifications using the APOGEE and *Gaia* parameters in this work compared to those inferred by Huber et al. (2014). Outliers from Fig. 14 are plotted as orange, green, and blue points. Median error bars for each class are shown in the right-hand side. *Right:* Same as left, except using stellar parameters derived from 2MASS colors by Huber et al. (2014).

In Fig. 14, we plot APOGEE  $T_{\text{eff}}$  against the 2MASS-based temperature calculated by Huber et al. (2014) for three regimes: cool dwarfs, hot stars and evolved stars. These regimes were defined coarsely: the cool dwarfs and evolved stars have APOGEE  $T_{\text{eff}} < 5250$  K and  $M_{K_s} > 2$  and  $M_{K_s} \leq 2$  respectively, the hot stars have APOGEE  $T_{\text{eff}} \geq 5250$  K. The classifications are illustrated in the left panel of Fig. 15. We flag stars with temperatures differing by  $4\sigma$  as outliers, and exclude them from the best-fit relations calculated in the comparison.

We find that the agreement between Huber et al. (2014) and APOGEE temperatures depends highly HR diagram position. For cool dwarfs, the slope of the temperature relation is nearly unity, but the Huber et al. (2014) temperatures are hotter than the APOGEE temperatures by 98 K. For the hot stars, the relationship between Huber et al. (2014) and APOGEE temperatures is more complex, as the slope is substantially different than one, likely reflecting that the 2MASS temperatures perform more poorly for the hotter stars, which is expected. We also note the presence of a small clump of six outlying points, plotted in orange. For the giant stars, both the slope and intercept are statistically indistinguishable from the one-to-one line, but there is a substantial residual corresponding to the red clump, which is resolved by APOGEE but not by Huber et al. (2014). In this regime we flag two sets of outliers, a set of six where the Huber et al. (2014) temperature is greater than APOGEE (shown in blue), and a set of nine outliers where the APOGEE temperature is higher (shown in

green). Of the 2,043 stars in the overlap sample between Huber et al. (2014) and APOGEE, only 21 are inconsistent outside the errors, or about a 1% discrepancy rate.

We also compare the evolutionary state classifications for *Gaia* and APOGEE to those inferred by Huber et al. (2014) using 2MASS colors. We estimate the Huber et al. (2014)-inferred *Ks*-band absolute magnitude by substituting the Huber et al. (2014) radius into the Stefan-Boltzmann law and applying a bolometric correction consistent with the Huber et al. (2014)  $T_{\text{eff}}$ . In Fig. 15, we find that gross misclassifications are extremely rare. First, we note that the orange outliers correspond directly to misclassified hot stars. We find that 5/1486 or 0.3% of Huber et al. (2014)-classified giants are grossly misclassified hot stars. There are no gross misclassifications of either cool stars or giants in the hot star domain. For stars whose Huber et al. (2014) parameters would classify them as cool dwarfs, 31/48, or 64%, of these stars are misclassified giants, which is to be expected as dwarfs overlap with giants in 2MASS colors. However, this disagreement is exaggerated by the dearth of cool stars in this sample compared to the full *Kepler* sample, and does not extend to the temperature estimates. Only 4 of the 31 misclassified red giants have 2MASS temperature estimates that differ substantially from the APOGEE temperature. We finally note that the remainder of the green outliers and all of the blue outliers have consistent evolutionary state classifications as giants, but simply have discrepant temperatures, indicating an outlier rate of 9/1486, or 0.6%.

#### B. PLEIADES CROSS-MATCHED SAMPLE

The cross-matched sample of Pleiades targets is given in Table 4 below.

